Available online at www.sciencedirect.com
ScienceDirect
Comput. Methods Appl. Mech. Engrg. 369 (2020) 113184
Computer methods in applied mechanics and engineering
www.elsevier.com/locate/cma

Computational thermomechanics for crystalline rock. Part II: Chemo-damage-plasticity and healing in strongly anisotropic polycrystals

Ran Ma, WaiChing Sun*

Department of Civil Engineering and Engineering Mechanics, Columbia University, 614 SW Mudd, Mail Code: 4709, New York, NY 10027, United States of America

Received 8 December 2019; received in revised form 25 May 2020; accepted 25 May 2020
Available online 13 June 2020

Abstract

We present a thermal–mechanical–chemical-phase field model that captures the multi-physical coupling effects of precipitation creeping, crystal plasticity, anisotropic fracture, and crack healing in polycrystalline rock at various temperature and strain-rate regimes. This model is solved via a fast Fourier transfer solver with an operator-split algorithm to update displacement, temperature and phase field, and chemical concentration incrementally. In nuclear waste disposal in salt formation, brine inside the crystal salt may migrate along the grain boundary and cracks due to the gradient of interfacial energy and pressure. This migration has a significant implication on the permeability evolution, creep deformation, and crack healing within rock salt but is difficult to incorporate implicitly via effective medium theories compared with computational homogenization. As such, we introduce a thermodynamic framework and a corresponding computational implementation that explicitly captures the brine diffusion along the grain boundary and crack at the grain scale. Meanwhile, the anisotropic fracture and healing are captured via a high-order phase field that represents the regularized crack region in which a newly derived non-monotonic driving force is used to capture the fracture and healing due to the solution–precipitation. Numerical examples are presented to demonstrate the capacity of the thermodynamic framework to capture the multiphysics material behaviors of rock salt.

Keywords: polycrystaline rock; precipitation creeping; phase field fracture; phase field healing; FFT Solver; nuclear waste disposal

1. Introduction

Rock salt formation has been widely considered as one of the potential repositories for nuclear waste disposal for decades. The design of these salt repositories often involves re-consolidated crushed salt as buffer or backfill materials to reduce excavation void space and the time required for the salt to close in around the nuclear waste. Due to the high thermal conductivity, the low permeability, the self-healing properties, and the ready availability of crushed salt in a repository, the re-consolidated crushed salt has attracted a significant amount of interest and becomes a major focus point in many studies by the US Department of Energy for heat-generating waste

* Corresponding author.
E-mail address: wsun@columbia.edu (W. Sun).

https://doi.org/10.1016/j.cma.2020.113184

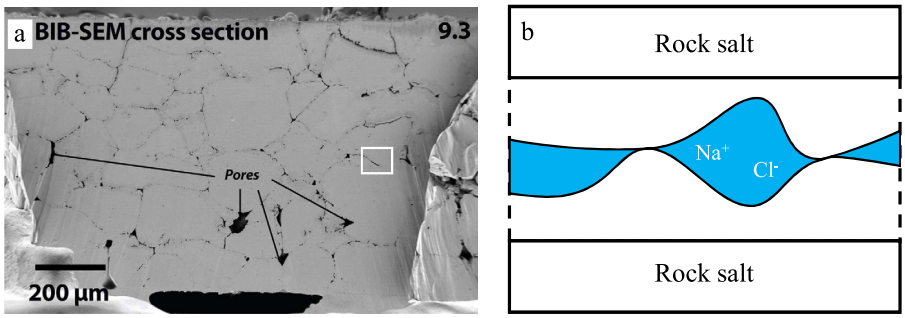

Fig. 1. Microstructure of rock salt with pores and intergranular brine: (a) SEM image [19]; (b) schematic illustration.

(e.g. Kuhlman [1],Martin et al. [2]). However, during the excavation, micro-cracks may form in the salt materials within the excavation damaged zone (EDZ) near the repository surface. Meanwhile, the reconsolidation of the crushed rock salt (which is often used as a backfill material) will also introduce defects and impurities such as brine, micro-cracks, pores, and a small amount of clay. These imperfections will evolve under thermal–mechanical loadings via different mechanisms, such as the deformation-induced perlocation [3], microcrack propagation [4], and crack healing [5–8]. To prevent leakage of the radioactive materials, it is necessary to understand how effective permeability of rock salt evolves under different temperatures and in situ stress.

This article is Part II of the paper series *Computational thermomechanics of crystalline rock*, preceded by Na and Sun [9], which focuses on the modeling of single-crystal salt. Our objective in this new contribution is to propose a computational framework for polycrystalline rock salt that explicitly captures the rate-dependent multi-physical coupling mechanisms that lead to a variety of anisotropic creeping, fracture, healing and plasticity under different temperature and pressure ranges at the mesoscale level. Due to the coupling nature of the healing, fracture, solution–precipitation creep, and heat transfer across length scales, it is difficult to derive macroscopic predictive models that capture the interactions of those complex mechanisms via phenomenological or even microstructure-inspired path-dependent material laws. As a result, our goal is to propose a model that directly simulate those multiphysics phenomena occurred at the polycrystalline microstructures, rather than introducing phenomenological constitutive laws for a homogenized effective medium [10,11].

1.1. Fracture and healing in rock salt: experimental evidence

The path-dependent deformation of polycrystalline rock salt is primarily dominated by three mechanisms across different length and time scales — dislocation creeping, solution–precipitation, and micro-cracking dilatancy [12]. The dislocation creep typically refers to the dislocation sliding along the slip planes or climbing perpendicular to the slip planes. Dislocation creep is the major deformation mechanism when the strain rate is larger than $1.0 \times 10^{-7}\,\mathrm{s}^{-1}$ [12]. When the strain rate is below $1.0 \times 10^{-7}\,\mathrm{s}^{-1}$, solution–precipitation becomes the major deformation mechanism due to the existence of intergranular brine. Fig. 1 shows the typical microstructure of a polycrystalline rock salt specimen with "island-channel" type grain boundaries. For a rock salt in a natural environment, the grain boundary regions are usually filled with saturated brine, which assists the solution–precipitation process. Meanwhile, the creeping due to intergranular solution–precipitation is the result of three sequential physical processes (cf. Kruzhanov and Stöckhert [13]): (1) the dissolution of solid phase across solid/liquid interface at high-pressure region; (2) the solute diffusion within intergranular brine due to the concentration gradient; and (3) the solute precipitation from brine to the solid phase at the low-pressure region. The efficiency of the solution–precipitation is pre-dominated by the slowest of these three sequential processes, which is diffusion rather than dissolution or precipitation for wet rock salt [14]. Therefore, solution–precipitation is largely influenced by pressure gradient [15], grain boundary structure [16], grain boundary misorientation [17], and concentration of aqueous trace metals [18].

The long-term creep behavior is also affected by the grain boundary or crack healing process [19], which not only reduces the permeability but also restores the stiffness [5]. Three major mechanisms account for crack healing [5,6]: (1) instantaneous mechanical closure due to increased grain boundary normal pressure; (2) diffusive crack-healing

driven by surface energy reduction; and (3) crack healing by recrystallization. Among these healing mechanisms, the diffusive crack healing driven by surface energy reduction is the most important in the long term crack healing of natural rock salt. Along with the pressure-induced solution–precipitation, the crack tip curvature also reduces the chemical potential of the solid phase, providing an additional driving force for precipitation [5,6,16]. The crack healing rate is controlled by solute diffusion instead of solution and precipitation [5], and the diffusivity within the thin film is measured [6]. Moreover, a detailed observation of the brine distribution in grain boundaries has revealed that the healed grain boundaries provide a threshold for the solution–precipitation process [19].

The deformation mechanism within the polycrystalline rock is so complicated that it is difficult for phenomenological based models to quantitatively describe dislocation creep, solution–precipitation, microcrack dilatancy, and crack healing simultaneously. Therefore, physics-based models and explicit representation of polycrystalline structure are necessary for a fundamental understanding and quantitative prediction of the deformation and permeability evolution within rock salt.

1.2. Fracture and healing in rock salt: material modeling

Numerous researches have been conducted toward a unified field formulation to predict multi-physical behaviors of rock salt and other crystalline rock. For instance, a self-consistent homogenization method is used such that the crystal plasticity simulations were upscaled to predict the anisotropic plastic deformation of polycrystalline rock salt [20,21]. A general kinematic framework was formulated to describe the diffusion and convection of brine and air inclusions within polycrystalline rock salt [22]. Kruzhanov and Stöckhert [13] modeled the solution–precipitation creep by introducing an inelastic displacement field that maximizes the creep deformation potential defined along the grain boundary. Front tracking technique and adaptive mesh technique are combined at the expense of numerical accuracy and efficiency to simulate grain boundary migration and diffusion in a Lagrangian framework by Bower and Wininger [23].

Predicting crack initiation, crack propagation, and crack healing within damaged rock salt through numerical simulations has received significant attention due to the ever-increasing demand for evaluating the permeability of crushed salt after re-consolidation. Crack healing has traditionally been considered within the framework of continuum damage mechanics [24,25]. A phenomenological model is proposed to describe the competitive effect between mechanical damage and healing in the excavation damaged zone (EDZ) through continuum damage mechanics [26]. More recently, this model is extended to capture the thermo-mechanical crack healing model to simulate the competition between mechanical damage and crack healing in rock salt [27]. Furthermore, the effect of solution–precipitation on the micropore healing process within polycrystalline rock salt is simulated by a diffusion-based homogenization model in Shen and Arson [28].

While those phenomenological models can replicate some aspects of the constitutive behaviors of rock salt, the number of material parameters required for curve-fitting is large and those material parameters often lack significant physical underpinnings and hence over-fitting may occur when those models are used for blind predictions [29–31]. To circumvent this situation, multiscale DEM–FEM or FEM^2 approaches are sometimes used to upscale the simplified microscopic behaviors from the grain scale to the macroscopic scale [10,32–35]. However, this upscaling procedure is only meaningful if the interplay of the coupled mechanisms such as microcracking dilatancy, solution–precipitation creeping, crack healing, crystal plasticity, and heat transfer can be sufficiently replicated at the grain scale. The objective of this paper is to provide this important theoretical framework and an FFT solver that *explicitly* captures these multi-physical coupling mechanisms, and as a result, enables us to explain, understand and upscaling these responses for macroscopic predictions.

1.3. Outlines, major contributions and notations

In this paper, a thermodynamic framework is proposed which explicitly incorporates crystal plasticity, solution–precipitation creep, strongly anisotropic cracking, and crack healing starting from the previous work [9]. The ductile plastic deformation and dislocation creeping of each crystal grain under different temperature and confining pressure are captured via crystal plasticity, whereas a high-order phase-field model is introduced to predict the anisotropic crack propagation in polycrystalline rock salt with a non-convex cleavage energy determined by the preferential fracture plane of rock salt. Meanwhile, the solution–precipitation creep is replicated by simulating the transport of

chemical species along the grain boundary. The chemical concentration then induces deformation. This approach is inspired by recent investigations that capture both Herring and Coble creeps at high homologous temperature [36–38]. In this work, our new contribution is that we incorporate this diffusion problem into a unified framework to predict how the solution–precipitation creep affects both the fracture and the healing process. Since the healing often starts at the crack tip, we introduce a measure of the curvature of the phase-field into our derivation of chemical potential such that the healing mechanism depends on the surface areas [5]. Finally, considering the high computational cost of the coupled equations and the global C_1 continuity requirement of the strongly anisotropic phase-field model, an FFT-based method is adopted to solve the coupled equations in an operator split manner.

This paper will proceed as follows. Section 2 discusses the balance law for mass, linear momentum, microforce, and energy, respectively. Section 3 presents the constitutive relation for small strain crystal plasticity, solution–precipitation, crack healing, and high-order phase-field. In Section 4, three examples are presented to demonstrate the capability of the proposed framework to represent the multiphysics behavior of rock salt in mesoscale. Section 5 summarizes the major results and concluding remarks.

As for notations and symbols, bold-faced letters denote tensors (including vectors which are rank-one tensors); the symbol '$\cdot$' denotes a single contraction of adjacent indices of two tensors (e.g. $\boldsymbol{a}\cdot\boldsymbol{b} = a_i b_i$ or $\boldsymbol{c}\cdot\boldsymbol{d} = c_{ij}d_{jk}$); the symbol ':' denotes a double contraction of adjacent indices of tensor of rank two or higher (e.g. $\boldsymbol{C} : \boldsymbol{\varepsilon^e} = C_{ijkl}\varepsilon^e_{kl}$); the symbol '::' denotes a fourth contraction of adjacent indices of tensor of rank four or higher (e.g. $\boldsymbol{C} :: \boldsymbol{D} = C_{ijkl}D_{ijkl}$); the symbol '$\otimes$' denotes a juxtaposition of two vectors (e.g. $\boldsymbol{a}\otimes\boldsymbol{b} = a_i b_j$) or two symmetric second order tensors (e.g. $(\boldsymbol{\alpha}\otimes\boldsymbol{\beta})_{ijkl} = \alpha_{ij}\beta_{kl}$); the symbol '$\mathcal{F}$' and '$\mathcal{F}^{-1}$' represent forward and backward Fourier transformation, respectively. Materials are assumed to possess cubic symmetry throughout this paper unless specified.

2. Balance laws

In this section, the governing equations of the thermal–mechanical–chemical-phase field framework are introduced. These equations constitute the boundary value problem that replicates the multiphysical material behaviors of polycrystalline rock salt in the geometrically linear regime. We first introduce an interfacial indicator function that defines the location of the grain boundary and regularized crack region. Then the balance principles for mass, linear momentum, and microforce (material force) are derived by extending the model in [9]. Finally, the energy balance equation and dissipation inequality are derived for the multiphysics problem.

2.1. Definition of interface region and indicator function

Cryogenic experiments have revealed the island—channel structure of the rock salt grain boundary region, where the saturated brine exists and solution–precipitation occurs [19]. The solution–precipitation in return will also influence the porosity of the grain boundary, and crack healing is enabled by the thin brine films within the crack region [39]. However, the morphology of the grain boundary region and the crack region is highly irregular and therefore difficult to capture via conformal meshes or embedded discontinuities [40,41]. To overcome this problem, we introduce regularized interfacial regions represented by phase fields to capture the multiphysical coupling process occurring along the grain boundary and the crack [36,42]. First, the indicator for the grain boundary region is introduced as

$$d_{\mathrm{GB}}(\boldsymbol{X}) = \begin{cases} 0, & \boldsymbol{X} \text{ in the lattice region} \\ 1, & \boldsymbol{X} \text{ in the grain boundary region,} \end{cases} \tag{1}$$

where $\boldsymbol{X}$ denotes the coordinate of the material point. A similar concept is also proposed in [16] to derive a theoretical model for solution–precipitation within rock salt. The indicator for the interfacial region (including grain boundary region and crack region) is defined as:

$$d_i\left(d_c, d_{\mathrm{GB}}\right) = 1 - \left[1 - d_c^2(\boldsymbol{X})\right]\left[1 - d_{\mathrm{GB}}^2(\boldsymbol{X})\right], \tag{2}$$

where $d_c(\boldsymbol{X}) \in [0, 1]$ is the phase field of the crack region. The square terms of the phase field d_c and the grain boundary indicator d_{GB} are consistent with Sharma et al. [42,43]. Note that in the numerical simulation, the value of d_{GB} within the grain interior region is a small positive number $0 < d_{\mathrm{GB}} \ll 1$ instead of exact zero to avoid singularity in the diffusion equation Eq. (42).

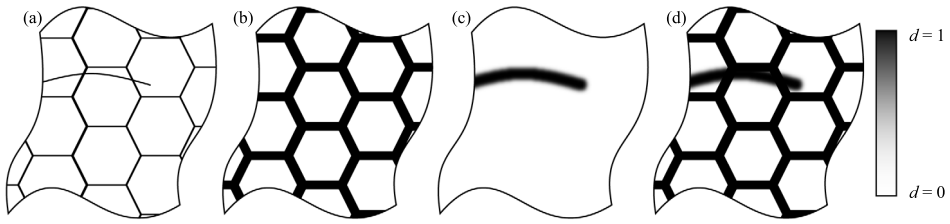

Fig. 2. A schematic representation of (a) A solid body Ω with crack discontinuity Γ_c and grain boundary discontinuity Γ_{GB}; (b) Grain boundary region Ω_{GB} with finite thickness and grain boundary indicator d_{GB}; (c) A regularized crack region Ω_c by fracture phase field d_c; (d) A regularized interfacial region $\Omega_i = \Omega_{GB} \cup \Omega_c$ by interfacial indicator d_i.

Consider a periodic domain Ω with n_{sd} the spatial dimensions, this domain Ω can be divided into the bulk region Ω_{bulk} and the interfacial region Ω_i through the interfacial indicator (see Fig. 2):

$$\Omega_{\text{bulk}} = \{\boldsymbol{X} | d_i(\boldsymbol{X}) < \text{tol}, \boldsymbol{X} \in \Omega\}, \quad \Omega_i = \{\boldsymbol{X} | d_i(\boldsymbol{X}) \geq \text{tol}, \boldsymbol{X} \in \Omega\}, \tag{3}$$

where tol $\in (0, 1)$ is a small enough positive number. The interfacial region contains the physical interface between the solid and liquid phase, and also involves plastic deformation at the solid–solid contact region [16].

The actual grain boundary of rock salt has an island-channel structure, as shown in Fig. 1. NaCl ions diffuse within the interfacial brine, together with mass transfer between the solid phase and liquid brine. The grain boundary thickness in numerical simulation should be chosen as a compromise between the real grain boundary, where solution–diffusion–precipitation occurs, and the computational cost. Previously, either $0.1\times$ grain size [36] or $4\,\mu$m [38] is used as the grain boundary thickness to simulate Coble creep. We choose $0.05\times$ grain size as the grain boundary thickness in this paper. .

2.2. Balance of mass

Let ρ_s denotes the intrinsic density of solid halite, ρ_l denotes the intrinsic density of brine, c denotes the intrinsic molar concentration of brine, and ϕ represents the local porosity of the interfacial domain. Let D/Dt denotes the material time derivative with respect to the solid phase, according to the mixture theory [44], the mass balance equations can be written as:

$$\begin{cases} \frac{D}{Dt}[(1-\phi)\rho_s] + (1-\phi)\rho_s \nabla^{\boldsymbol{x}} \cdot \boldsymbol{v} = -\phi r_c M, & \text{in } \Omega_i \\ \frac{D}{Dt}(\phi\rho_l) + \phi\rho_l \nabla^{\boldsymbol{x}} \cdot \boldsymbol{v} + \nabla^{\boldsymbol{x}} \cdot [\phi\rho_l(\boldsymbol{v}_l - \boldsymbol{v})] = \phi r_c M, & \text{in } \Omega_i \\ \frac{D}{Dt}(\phi c) + \phi c \nabla^{\boldsymbol{x}} \cdot \boldsymbol{v} + \nabla^{\boldsymbol{x}} \cdot [\phi\rho_l(\boldsymbol{v}_l - \boldsymbol{v}) + \boldsymbol{J}] = \phi r_c, & \text{in } \Omega_i. \end{cases} \tag{4}$$

Here, $\boldsymbol{v}$ is the velocity of the solid phase, $\boldsymbol{v}_l$ is the velocity of the liquid phase, $\boldsymbol{J}$ is the diffusion flux, r_c is the molar dissolution rate, and M is the molar mass of halite.

We made several assumptions to simplify the mass balance equations. First, we assume that the bulk porosity ϕ remains constant in time scale and homogeneous in the spatial domain. Furthermore, the material parameters are measured from upscaling a representative elementary volume which may contain voids. However, the diffusivity of the crystalline material is mainly attributed to the interconnected interface domain, i.e. the grain boundaries and the cracks, which can be identified from the interfacial indicator d_i [45]. To further simplify the model, we follow the treatment in Garikipati et al. [36] and Villani et al. [38], which assume that the volumetric strain of the solid constituent (and hence the porosity change) and the divergence of the Darcy's velocity $(\boldsymbol{v}_l - \boldsymbol{v})$ have negligible effect on the solution–precipitation creep rate, the change of the liquid density and the specie concentration. While incorporating the effect of the porosity change and the fluid flux terms could be important for leakage or for high porosity rock salt, such an extension is out of the scope of this study and will be considered in the future. As a result, the mass balance equations (4) can be simplified as:

$$\begin{cases} \dot{\boldsymbol{\varepsilon}}^c = -r_c \Omega_v \boldsymbol{n} \otimes \boldsymbol{n}, & \text{in } \Omega_i \\ \dot{\rho}_l = r_c M, & \text{in } \Omega_i \\ \dot{c} + \nabla^{\boldsymbol{x}} \cdot \boldsymbol{J} = r_c, & \text{in } \Omega_i. \end{cases} \tag{5}$$

In this equation, $\dot{\boldsymbol{\varepsilon}}^c$ is the solution–precipitation creep rate, Ω_v is the molar volume of solid rock salt, and $\boldsymbol{n}$ is the normal direction of the interfacial region. The solution–precipitation creep rate $\dot{\boldsymbol{\varepsilon}}^c$ is also used to model Coble creep deformation within the grain boundary region [36–38]. The mass flux $\boldsymbol{J}$ is a function of the chemical potential gradient. The source term r_c is proportional to the difference between the equilibrium concentration c_{eq} and the brine concentration c, as illustrated in Section 3.2.

2.3. Balance of linear momentum and microforce

To complete the field theory, the balance laws of linear momentum and microforce (material force) are briefly summarized. While the balance of linear momentum constrains the stress field, the microforce balance provides an additional governing equation for the degradation evolution within the crystal grains and grain boundaries (cf. Na and Sun [9]). Moreover, microforce corresponding to the second-order gradient of phase-field is introduced to incorporate the strongly anisotropic fracture observed in rock salt.

First, it is assumed throughout this paper that all the governing equations and corresponding physical quantities are defined in a cubic shape representative volume element (RVE) with periodic boundary conditions, and no body force or inertia force is considered. As a result, the balance of linear momentum requires that the divergence of the Cauchy stress σ vanishes everywhere:

$$\nabla^{\boldsymbol{x}} \cdot \boldsymbol{\sigma} = \boldsymbol{0}. \tag{6}$$

The Cauchy stress $\boldsymbol{\sigma}$ is, under small strain assumption, power-conjugate with the infinitesimal strain rate $\dot{\boldsymbol{\varepsilon}}$. The strain energy equivalence principle is adopted here to simplify the coupling relationship between the phase field and the Cauchy stress, where we assume that a fictitious undamaged body exists with possibly unbalanced linear momentum corresponding to the damaged counterpart. The total stress $\boldsymbol{\sigma}$ within the damaged body and the effective stress $\hat{\boldsymbol{\sigma}}$ within the undamaged body are assumed to be co-axial and can be related by introducing a scalar degradation function $g(d_c)$, defined as

$$\boldsymbol{\sigma} = g(d_c)\hat{\boldsymbol{\sigma}}, \quad g(d_c) = (1-k)(1-d_c)^2 + k \tag{7}$$

where $0 < k \ll 1$ represents the residual portion of stiffness within the damaged region to retain the well-posedness of the problem. Note that the degradation function $g(d_c)$ is an isotropic function of the phase field d_c, so that the fictitious effective stress $\hat{\boldsymbol{\sigma}}$ and the actual stress $\boldsymbol{\sigma}$ are coaxial. The phase field anisotropy is incorporated in the phase field free energy ψ^d in Eq. (24).

The existence of microforce power conjugate to the phase-field is postulated together with the balance law for the microforce, such that the phase-field theory can be incorporated into the coupling equations with thermodynamic consistency [46]. Supposing that π, $\boldsymbol{\xi}$, and $\boldsymbol{\eta}$ are the microforces power conjugate to the phase field $\dot{d}_c$ and its first $\nabla^{\boldsymbol{x}}\dot{d}_c$ and second order gradient $\nabla^{\boldsymbol{x}}\nabla^{\boldsymbol{x}}\dot{d}_c$ respectively, then the balance law of the microforces requires that

$$\pi - \nabla^{\boldsymbol{x}} \cdot \boldsymbol{\xi} + (\nabla^{\boldsymbol{x}}\nabla^{\boldsymbol{x}}) : \boldsymbol{\zeta} = 0. \tag{8}$$

It is also assumed that the body force of the microforces vanishes.

The anisotropic microfracture can be incorporated into the crystal plasticity model to predict the brittle–ductile transition in rocks [47]. Here, we try to model the microcrack propagation explicitly in order to provide a deep understanding of the multi-physics material process within rock salt. Note that in our previous work [9], multi-phase-field is adopted for strongly anisotropic fracture. While this approach is feasible to replicate strongly anisotropic fracture, the introduction of multiple phase fields may significantly increase the computational resources required to solve the problems numerically. To improve efficiency, we have adopted the higher-order phase field fracture model (cf. Li et al. [48],Li and Maurini [49] where only one phase field is required to replicate the strong anisotropy. The global continuity of the interpolated phase field required to resolve the higher-order terms is fulfilled by the trigonometric function basis of the FFT model [50].

2.4. Balance of energy and dissipation inequality

In this section, the thermodynamic laws are presented in terms of the mechanical work, structural heating, crack surface energy, and chemical potential. Our starting point is the derivation from Na and Sun [9] with the following

improvements and modifications. (1) A high-order phase-field is introduced to replace the multi-phase-field to improve computational efficiency and to reduce the number of material parameters. (2) The dissipation due to fluid diffusion as well as those due to dissolution and precipitation are incorporated in the formulation to model the solution–precipitation creeping and crack healing.

The total infinitesimal strain $\boldsymbol{\varepsilon}$ is therefore decomposed into three parts:

$$\boldsymbol{\varepsilon} = \boldsymbol{\varepsilon}^e + \boldsymbol{\varepsilon}^p + \boldsymbol{\varepsilon}^c, \tag{9}$$

where $\boldsymbol{\varepsilon}^e$ is the elastic strain, $\boldsymbol{\varepsilon}^p$ is the plastic strain, and $\boldsymbol{\varepsilon}^c$ is the strain caused by the solution and precipitation of intergranular brine.

Define e as the internal energy per unit volume. The first law of thermodynamics requires that the internal energy changing rate $\dot{e}$ equals to the total energy input rate:

$$\dot{e} = \boldsymbol{\sigma} : \dot{\boldsymbol{\varepsilon}} - \nabla^{\boldsymbol{x}} \cdot \boldsymbol{q} + r_\theta + \pi \dot{d}_c + \boldsymbol{\xi} \cdot \nabla^{\boldsymbol{x}} \dot{d}_c + \boldsymbol{\zeta} : \left(\nabla^{\boldsymbol{x}} \nabla^{\boldsymbol{x}} \dot{d}_c\right) + \mu \dot{c} - \boldsymbol{J} \cdot \nabla^{\boldsymbol{x}} \mu + (\mu_{se} - \mu)\, r_c, \tag{10}$$

where $\boldsymbol{q}$ is the thermal flux, r_θ is the heat source, μ is the chemical potential of the salt solute within the intergranular brine, and μ_{se} is the chemical potential of the rock salt in solid phase. The thermal, mechanical, and chemical part of the external energy input rate is consistent with Gurtin et al. [51] and Anand [52]. The internal energy corresponding to the phase field and its gradient is consistent with Part I of this paper series [9], except that the high order term $\boldsymbol{\zeta} : \left(\nabla^{\boldsymbol{x}} \nabla^{\boldsymbol{x}} \dot{d}_c\right)$ is introduced for strong anisotropy. The internal energy changing rate due to solution and precipitation across the solid–liquid interface $(\mu_{se} - \mu)\, r_c$ is also incorporated similar to the model for Li ions battery [53] and polycrystalline rock [54]. Here, the chemical potential of the solid phase μ_{se} is a function of the stress and the solid–liquid interfacial radius [16,54], as shown in Eq. (39). Furthermore, the Clausius–Duhem inequality takes the following form [51]:

$$\int_V \left(\dot{\eta} - \frac{r_\theta}{\theta}\right) \mathrm{d}V + \int_{\partial V} \left(\frac{\boldsymbol{q}}{\theta}\right) \cdot \boldsymbol{n}\, \mathrm{d}S \geq 0, \tag{11}$$

where η is the entropy per unit volume, and V is an arbitrary domain within Ω with $\boldsymbol{n}$ represents the outward-pointing normal direction. The local form of the Clausius–Duhem inequality Eq. (11) reads:

$$\dot{\eta} \geq -\nabla^{\boldsymbol{x}} \cdot \left(\frac{\boldsymbol{q}}{\theta}\right) + \frac{r_\theta}{\theta}. \tag{12}$$

Consider that the energy balance equation Eq. (10) can be re-written as:

$$\begin{aligned} -\nabla^{\boldsymbol{x}} \cdot \left(\frac{\boldsymbol{q}}{\theta}\right) + \frac{r_\theta}{\theta} =& \frac{1}{\theta}\left(-\nabla^{\boldsymbol{x}} \cdot \boldsymbol{q} + r_\theta\right) + \frac{1}{\theta^2} \boldsymbol{q} \cdot \nabla^{\boldsymbol{x}} \theta \\ =& \frac{1}{\theta}\Big[\, \dot{e} - \boldsymbol{\sigma} : \dot{\boldsymbol{\varepsilon}} + \frac{1}{\theta} \boldsymbol{q} \cdot \nabla^{\boldsymbol{x}} \theta - \pi \dot{d}_c - \boldsymbol{\xi} \cdot \nabla^{\boldsymbol{x}} \dot{d}_c - \boldsymbol{\zeta} : \left(\nabla^{\boldsymbol{x}} \nabla^{\boldsymbol{x}} \dot{d}_c\right) \\ & - \mu \dot{c} + \boldsymbol{J} \cdot \nabla^{\boldsymbol{x}} \mu - (\mu_{se} - \mu)\, r_c \,\Big], \end{aligned} \tag{13}$$

the local entropy inequality Eq. (12) can be re-written by substituting the above equation as:

$$\dot{e} - \theta \dot{\eta} - \boldsymbol{\sigma} : \dot{\boldsymbol{\varepsilon}} + \frac{1}{\theta} \boldsymbol{q} \cdot \nabla^{\boldsymbol{x}} \theta - \pi \dot{d}_c - \boldsymbol{\xi} \cdot \nabla^{\boldsymbol{x}} \dot{d}_c - \boldsymbol{\zeta} : \left(\nabla^{\boldsymbol{x}} \nabla^{\boldsymbol{x}} \dot{d}_c\right) - \mu \dot{c} + \boldsymbol{J} \cdot \nabla^{\boldsymbol{x}} \mu - (\mu_{se} - \mu)\, r_c \leq 0. \tag{14}$$

The Helmholtz free energy ψ is introduced through the Legendre transformation of the internal energy e as:

$$\psi = e - \theta \eta. \tag{15}$$

Then, the local entropy inequality Eq. (14) can be written as the free energy inequality:

$$\dot{\psi} - \eta \dot{\theta} - \boldsymbol{\sigma} : \dot{\boldsymbol{\varepsilon}} + \frac{1}{\theta} \boldsymbol{q} \cdot \nabla^{\boldsymbol{x}} \theta - \pi \dot{d}_c - \boldsymbol{\xi} \cdot \nabla^{\boldsymbol{x}} \dot{d}_c - \boldsymbol{\zeta} : \left(\nabla^{\boldsymbol{x}} \nabla^{\boldsymbol{x}} \dot{d}_c\right) - \mu \dot{c} + \boldsymbol{J} \cdot \nabla^{\boldsymbol{x}} \mu - (\mu_{se} - \mu)\, r_c \leq 0. \tag{16}$$

We assume that the Helmholtz free energy ψ takes the general form:

$$\psi = \psi\left(\boldsymbol{\varepsilon}^e, d_c, \nabla^{\boldsymbol{x}} d_c, \nabla^{\boldsymbol{x}} \nabla^{\boldsymbol{x}} d_c, c, \theta\right), \tag{17}$$

following the treatment in Anand [55] where the free energy ψ is assumed to be independent of the internal variable $\tilde{\tau}$. Then, the free energy inequality Eq. (16) can be written as

$$\begin{aligned}\mathcal{D} = &\left(\boldsymbol{\sigma} - \frac{\partial \psi}{\partial \boldsymbol{\varepsilon}^e}\right) : \dot{\boldsymbol{\varepsilon}}^e + \boldsymbol{\sigma} : \dot{\boldsymbol{\varepsilon}}^p - \left(\eta + \frac{\partial \psi}{\partial \theta}\right)\dot{\theta} - \frac{1}{\theta}\boldsymbol{q} \cdot \nabla^{\boldsymbol{x}}\theta \\ &+ \left(\pi - \frac{\partial \psi}{\partial d_c}\right)\dot{d}_c + \left(\boldsymbol{\xi} - \frac{\partial \psi}{\partial \nabla^{\boldsymbol{x}} d_c}\right) \cdot \nabla^{\boldsymbol{x}}\dot{d}_c + \left(\boldsymbol{\zeta} - \frac{\partial \psi}{\partial \left(\nabla^{\boldsymbol{x}}\nabla^{\boldsymbol{x}}\dot{d}_c\right)}\right) : \left(\nabla^{\boldsymbol{x}}\nabla^{\boldsymbol{x}}\dot{d}_c\right) \\ &+ \left(\mu - \frac{\partial \psi}{\partial c}\right)\dot{c} - \boldsymbol{J} \cdot \nabla^{\boldsymbol{x}}\mu + \boldsymbol{\sigma} : \dot{\boldsymbol{\varepsilon}}^c + \left(\mu_{se} - \mu\right) r_c \geq 0.\end{aligned} \tag{18}$$

According to the Coleman–Noll argument, the arbitrary changing rate of the state variables $\dot{\boldsymbol{\varepsilon}}^e$, $\dot{\theta}$, and $\dot{c}$ requires that:

$$\boldsymbol{\sigma} = \frac{\partial \psi}{\partial \boldsymbol{\varepsilon}^e}, \quad \eta = -\frac{\partial \psi}{\partial \theta}, \quad \mu = \frac{\partial \psi}{\partial c}. \tag{19}$$

Furthermore, the arbitrariness of the phase field $\dot{d}_c$ and its gradient $\nabla^{\boldsymbol{x}}\dot{d}_c$ and $\left(\nabla^{\boldsymbol{x}}\nabla^{\boldsymbol{x}}\dot{d}_c\right)$ requires that:

$$\pi = \frac{\partial \psi}{\partial d_c}, \quad \boldsymbol{\xi} = \frac{\partial \psi}{\partial \nabla^{\boldsymbol{x}} d_c}, \quad \boldsymbol{\zeta} = \frac{\partial \psi}{\partial \left(\nabla^{\boldsymbol{x}}\nabla^{\boldsymbol{x}}\dot{d}_c\right)}. \tag{20}$$

With the Coleman–Noll argument Eqs. (19) and (20), the dissipation inequality Eq. (18) can be simplified as:

$$\mathcal{D} = \underbrace{\boldsymbol{\sigma} : \dot{\boldsymbol{\varepsilon}}^p}_{\mathcal{D}_{loc}} \underbrace{-\frac{1}{\theta}\boldsymbol{q} \cdot \nabla^{\boldsymbol{x}}\theta}_{\mathcal{D}_{con}} \underbrace{-\boldsymbol{J} \cdot \nabla^{\boldsymbol{x}}\mu}_{\mathcal{D}_{diff}} + \underbrace{\boldsymbol{\sigma} : \dot{\boldsymbol{\varepsilon}}^c + \left(\mu_{se} - \mu\right) r_c}_{\mathcal{D}_{tran}} \geq 0, \tag{21}$$

where $\mathcal{D}_{\text{loc}}$ represents the mechanical dissipation, $\mathcal{D}_{\text{con}}$ represents the thermal conduction dissipation, $\mathcal{D}_{\text{diff}}$ represents the diffusion dissipation, and $\mathcal{D}_{\text{tran}}$ represents the dissipation due to dissolution and precipitation.

A sufficient condition for the total dissipation $\mathcal{D}$ to be non-negative is that all the dissipation components are non-negative individually. The diffusion dissipation and solution–precipitation dissipation are given by

$$\begin{cases} \mathcal{D}_{\text{diff}} &= -\boldsymbol{J} \cdot \nabla^{\boldsymbol{x}}\mu \geq 0 \\ \mathcal{D}_{\text{tran}} &= \boldsymbol{\sigma} : \dot{\boldsymbol{\varepsilon}}^c + r_c\left(\mu_{se} - \mu\right) = r_c\left[\mu_{se} - \mu - \Omega_v \boldsymbol{\sigma} : (\boldsymbol{n} \otimes \boldsymbol{n})\right] \geq 0. \end{cases} \tag{22}$$

These two inequality conditions pose restrictions to the admissible mass diffusion and solution–precipitation constitutive relations as shown in Section 3.2. The thermal conduction dissipation $\mathcal{D}_{\text{con}}$ is guaranteed positive by the Fourier's law and a positive scalar thermal conductivity κ (or a positive definite thermal conductivity tensor). The Fourier's law is used to correlate the heat flux $\boldsymbol{q}$ and the temperature θ:

$$\boldsymbol{q} = -\kappa \nabla^{\boldsymbol{x}}\theta \tag{23}$$

where the scalar variable κ is the isotropic thermal conductivity.

2.5. A specific form of free energy

The following expression is adopted for the total free energy ψ, which is split into the elastic free energy ψ^e, the crack surface energy ψ^d, the chemical free energy ψ^c, and the thermal contribution of the stored energy ψ^θ:

$$\psi = \psi^e(\boldsymbol{\varepsilon}^e, \theta, d_c) + \psi^d(d_c, \nabla^{\boldsymbol{x}} d_c, \nabla^{\boldsymbol{x}}\nabla^{\boldsymbol{x}}\dot{d}_c) + \psi^c(c, \theta) + \psi^\theta(\theta). \tag{24}$$

A specific form of free energy is proposed based on our previous work [9] with the following modifications: (1) Chemical free energy ψ^c is included for solute diffusion within interfacial brine; (2) High-order phase-field cleavage energy is used instead of multi-phase-field cleavage energy; (3) An initial phase-field penalizing term is included to avoid the sharp material contrast between the crack region and the intact region. The five parts of the

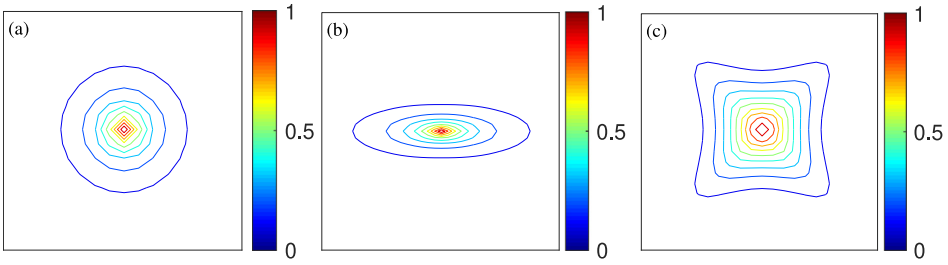

Fig. 3. Phase field distribution when the phase field value at the center is enforced as unity. The phase field distributions minimize the total phase field free energy ψ^d. (a) Phase field distribution corresponding to isotropic phase field free energy ($\mathbb{A} = \mathbb{I}$); (b) Phase field distribution corresponding to low-order phase field, where phase field is a convex function with one preferential cleavage direction [50]; (c) Phase field distribution corresponding to high-order phase field in Eq. (25), where phase field is a non-convex function with two perpendicular preferential cleavage directions determined by the fourth order anisotropic tensor $\mathbb{A}$.

Helmholtz free energy ψ take the following form:

$$\begin{cases} \psi^e = & g(d_c)w_+^e(\varepsilon^e,\theta) + w_-^e(\varepsilon^e,\theta) \\ \psi^d = & G_c\left[\frac{1}{2l_0}d_c^2 + \frac{l_0}{4}\nabla^{\boldsymbol{x}}d_c\cdot\nabla^{\boldsymbol{x}}d_c + \frac{l_0^3}{32}\left(\nabla^{\boldsymbol{x}}\nabla^{\boldsymbol{x}}\dot{d}_c\right):\mathbb{A}:\left(\nabla^{\boldsymbol{x}}\nabla^{\boldsymbol{x}}\dot{d}_c\right) + \frac{1}{2}\beta_{ipf}\left(d_c-1\right)^2\right] \\ \psi^c = & \mu_0 c + R\theta c\left(\ln\frac{c}{c_0} - 1\right) \\ \psi^\theta = & c_v\left[(\theta-\theta_0) - \theta\ln(\theta/\theta_0)\right] \end{cases} \tag{25}$$

Here, G_c is the cleavage energy per unit mass, l_0 is the character length, β_{ipf} is the penalty coefficient for the initial phase field, θ_0 is the initial temperature, and c_v is the specific heat coefficient per unit mass. The 4th order tensor $\mathbb{A}$ makes the phase field free energy ψ^d an anisotropic function of the phase field d_c as shown in Fig. 3, where the spatial distribution of the phase field d_c is a non-convex function with two preferential cleavage direction. The isotropic phase field free energy ψ^d can be recovered by replacing $\mathbb{A}$ with the 4th order identity tensor $\mathbb{I}$. Note that in the mesoscale Coble creep models, either statistical thermodynamics based chemical free energy density ψ^c [36] or classical lattice-void free energy density ψ^c [37,38] is utilized. For the interfacial brine, the chemical free energy density ψ^c for ideal fluid is used, although other choices remain applicable.

The positive part w_+^e and negative part w_+^e of the elastic strain energy in equation Eq. (25) are also defined to avoid crack propagation under volumetric compression:

$$\begin{cases} w_+^e = \frac{1}{2}K\langle\varepsilon_v^e\rangle_+^2 + \mu\left(\boldsymbol{\varepsilon}_d^e:\boldsymbol{\varepsilon}_d^e\right) - 3\alpha K(\theta-\theta_0)\langle\varepsilon_v^e\rangle_+ \\ w_-^e = \frac{1}{2}K\langle\varepsilon_v^e\rangle_-^2 - 3\alpha K(\theta-\theta_0)\langle\varepsilon_v^e\rangle_-, \end{cases} \tag{26}$$

where ε_v^e is the volumetric elastic strain, $\boldsymbol{\varepsilon}_d^e$ is the deviatoric elastic strain, α is the thermal expansion coefficient, and K and μ are Lamé constants.

To further simplify the balance of energy equation, we assume that the entropy change due to chemical diffusion and crack propagation is negligible compared with plastic dissipation, such that:

$$\theta\frac{\partial^2\psi}{\partial\theta\partial c}\dot{c} = R\theta\ln\frac{c}{c_0}\dot{c} \ll \mathcal{D}_{\text{loc}}, \quad \theta\frac{\partial^2\psi}{\partial\theta\partial d_c}\dot{d}_c = -3\alpha\theta K g'(d_c)\langle\varepsilon_v^e\rangle_+\dot{d}_c \ll \mathcal{D}_{\text{loc}}. \tag{27}$$

Substitute the Legendre transformation Eq. (15) and the specific form of free energy ψ Eq. (24) into the energy balance equation (Eq. (10)), and consider the Coleman–Noll arguments (Eq. (19)) and (Eq. (20)) and the above equation, the energy balance equation can be written as:

$$c_v\dot{\theta} = \theta\frac{\partial^2\psi}{\partial\theta\partial\boldsymbol{\varepsilon}^e}:\dot{\boldsymbol{\varepsilon}}^e + \boldsymbol{\sigma}:\dot{\boldsymbol{\varepsilon}}^p - \nabla^{\boldsymbol{x}}\cdot\boldsymbol{q} + r_\theta = -3\alpha K\theta\boldsymbol{I}:\dot{\boldsymbol{\varepsilon}}^e + \boldsymbol{\sigma}:\dot{\boldsymbol{\varepsilon}}^p - \nabla^{\boldsymbol{x}}\cdot\boldsymbol{q} + r_\theta. \tag{28}$$

Considering that the phase field d_c is non-conserved and brittle fracture (instead of creep damage) is rate-independent, Ginzburg–Landau type phase-field equation is derived based on the specific form of free energy ψ(24). Substitute the Coleman–Noll relation (20) into the microscopic force balance equation (8), and assuming that the

fourth order anisotropic tensor $\mathbb{A}$ is piecewise constant:

$$\frac{G_c}{l_0}d_c - \frac{G_c l_0}{2}\nabla^{\boldsymbol{x}}\cdot\nabla^{\boldsymbol{x}}d_c + \frac{G_c l_0^3}{16}\mathbb{A}::\nabla^4 d_c + \beta_{ipf}\left(d_c-1\right) = 2\left(1-d_c\right)\mathcal{H}, \quad d_c \in H^4_{\#}, \tag{29}$$

where $H^4_{\#}$ denotes the Sobolev space of Ω-periodic functions [56]. Note that the 4th order gradient of the phase field d_c exists in the strong form Eq. (29), the 4th order derivative of the solution field should be quadratically integrable. Here, the phase field driving force $\mathcal{H}$ is a function of the fictitious stored strain energy without degradation:

$$\mathcal{H} = \max_{\tau\in[0,t]}\left(w^e_+\right), \tag{30}$$

where the positive part of the elastic stored energy w^e_+ and the accumulated plastic work w^p will be introduced in the following section. The Macaulay brackets $\langle\cdot\rangle$ represent the ramp function. The plastic deformation threshold w^p_0 is introduced to control the contribution from accumulated plastic work w^p to ductile fracture. Note that the phase-field driving force $\mathcal{H}$ in Eq. (30) is monotonically increasing, which will be modified in Section 3.3 to enable diffusion controlled crack healing.

3. Constitutive relations

This section introduces the constitutive relations used in this paper. First, a small strain crystal plasticity model is revisited with a Voce type hardening relation. Then, a diffusion model is introduced which allows the solution, diffusion, and precipitation of NaCl solute along the grain boundary region and the crack region. Chemical potential depending on pressure and solid/liquid interface curvature is considered which enables pressure gradient driven and crack tip driven solution and precipitation. Finally, a fourth-order anisotropic tensor representing the preferential cleavage direction is presented for the high-order phase-field model, together with a modified phase-field driving force to enable diffusion-controlled crack healing.

3.1. Small strain crystal plasticity

The current small strain crystal plasticity model is re-formulated based on the finite strain counterpart [57,58]. The elastic constitutive relation is derived based on the effective stress $\hat{\boldsymbol{\sigma}}$ defined in Eq. (7), the additive decomposition in Eq. (9), the Coleman–Noll argument in Eq. (19), and the elastic free energy in Eq. (25) as:

$$\hat{\boldsymbol{\sigma}} = \hat{\boldsymbol{C}} : \boldsymbol{\varepsilon}^e, \quad \boldsymbol{\varepsilon}^e = \boldsymbol{\varepsilon} - \boldsymbol{\varepsilon}^p - \boldsymbol{\varepsilon}^c \tag{31}$$

where $\boldsymbol{\sigma}$ is the Cauchy stress, $\boldsymbol{\varepsilon}$ is the total strain rate, $\boldsymbol{\varepsilon}^\theta$ is the thermal expansion, $\boldsymbol{\varepsilon}^c$ is the chemical deformation, and $\boldsymbol{C}$ is the 4th order elastic stiffness tensor. The chemical deformation is an explicit function of the solution–precipitation rate r_c, as defined in Eq. (5).

In polycrystalline material, the plastic strain is achieved by dislocation slide on each slip system. Let $\boldsymbol{n}^{(s)}$ and $\boldsymbol{b}^{(s)}$ represent the normal and slip direction of the (s) th slip system, Then the total plastic strain is the tensorial summation of the shear strain on each slip system:

$$\dot{\boldsymbol{\varepsilon}}^p = \sum_{s=1}^{n_{slip}} \dot{\gamma}^{(s)}\boldsymbol{m}^{(s)}, \quad \boldsymbol{m}^{(s)} = \mathrm{sym}\left(\boldsymbol{b}^{(s)}\otimes\boldsymbol{n}^{(s)}\right). \tag{32}$$

For small strain problem, the anti-symmetric part of the slip system does not contribute to the plastic strain.

In this investigation, the Voce model is adopted as the constitutive relation considering that rock salt is strain rate sensitive. Note that the Voce model is temperature independent, and temperature dependence can be introduced by replacing the Voce model by other crystal plasticity models such as the mechanical threshold (MTS) model [59]. The relationship between the shear strain rate of the (s) th slip system $\dot{\gamma}^{(s)}$ and the resolved shear stress $\tau^{(s)}$ is assumed to follow the power law:

$$\dot{\gamma}^{(s)} = \frac{\dot{\gamma}_0}{\tilde{\tau}}\left|\frac{\tau^{(s)}}{\tilde{\tau}}\right|^{n-1}\tau^{(s)}. \tag{33}$$

Here, $\dot{\gamma}_0$ is the reference slip rate, and $\tilde{\tau}$ is the isotropic hardening variable. In this model, Taylor hardening is assumed where all slip systems contribute equally to the hardening variable $\tilde{\tau}$. The slip system resistance $\tilde{\tau}$ is decomposed into the intrinsic (yield) resistance τ_y and the extrinsic (hardening) resistance τ_w

$$\tilde{\tau} = \tau_y + \tau_w. \tag{34}$$

The extrinsic resistance τ_w evolves as a function of the slip system activity $\dot{\gamma}^{(s)}$

$$\dot{\tau}_w = h_0 \left(1 - \frac{\tau_w}{\tau_v}\right)^m \sum_{s=1}^{n_{slip}} \left|\dot{\gamma}^{(s)}\right| \tag{35}$$

where θ_0 is the initial hardening rate, and the work hardening saturation strength τ_v sets the upper bound of τ_w. The exponents m and n are separate parameters. Note that the hardening variable $\tilde{\tau}$ is monotonically increasing, so the current crystal plasticity model is not suitable for creep loading. Dislocation creep deformation can be modeled by introducing a dislocation annihilation model [60].

3.2. Constitutive relation for interfacial diffusion

This section provides the derivation of the constitutive relation for the diffusion problem. To capture the fully coupled chemical–mechanical effect, the constitutive relation for the chemical potential μ is derived from a corresponding Gibbs free energy [36]. We assume that the chemical potential of the solute in brine does not explicitly depend on stress. Hence, the chemical potential μ [unit: J mol^{-1}] for ideal solution is derived based on the Coleman–Noll argument Eq. (19) and the chemical free energy Eq. (25) as:

$$\mu = \mu_0 + R\theta \ln \frac{c}{c_0}, \quad \nabla^{\boldsymbol{x}} \mu = \frac{R\theta}{c} \nabla^{\boldsymbol{x}} c + R \ln \frac{c}{c_0} \nabla^{\boldsymbol{x}} \theta, \tag{36}$$

where μ_0 and c_0 are the reference chemical potential and reference concentration, respectively.

The diffusion of brine along grain boundaries and cracks contributes to the solution–precipitation creep and crack healing. It is assumed that the diffusion coefficient D_0 is independent of the grain boundary normal pressure, so that the diffusion equation remains linear. Assuming that the temperature-gradient driven diffusion is negligible compared with the concentration-gradient driven diffusion, the flux of the salt solution $\boldsymbol{J}$ along the grain boundary is proportional to the gradient of the chemical potential μ, i.e.,

$$\boldsymbol{J} = -\frac{d_i\left(d_c, d_{\mathrm{GB}}\right) D_0 c}{R\theta} \nabla^{\boldsymbol{x}} \mu = -d_i\left(d_c, d_{\mathrm{GB}}\right) D_0 \nabla^{\boldsymbol{x}} c \tag{37}$$

where D_0 [unit: mm^2 s^{-1}] is the diffusion coefficient of saturated salt solution. This diffusion coefficient D_0 is a positive scalar such that the diffusion dissipation $\mathcal{D}_{\mathrm{diff}}$ is non-negative. The interface indicator $d_i\left(d_c, d_{\mathrm{GB}}\right)$ ensures that the diffusion flux outside the interfacial region Ω_i approximately vanishes [42].

Assuming that the brine concentration is close to the halite equilibrium concentration c_{eq}, the solution–precipitation rate r_c is proportional to the difference between the equilibrium concentration c_{eq} and current concentration c based on the experimental observations on mineral solution–precipitation [15,18]:

$$r_c = d_i\left(d_c, d_{\mathrm{GB}}\right) \alpha_s k_s \left(c_{eq} - c\right), \tag{38}$$

where α_s [unit: mm^{-1}] is a material coefficient which is inversely proportional to the grain boundary thickness, and k_s [unit: mm s^{-1}] is the solution–precipitation coefficient which denotes the speed of salt migrating across the solid/liquid interface. Note that the solution coefficient k_s is positive such that the second part of $\mathcal{D}_{\mathrm{tran}} \geq 0$. In Eq. (38), the equilibrium concentration c_{eq} depends on the pressure, temperature, and solid/liquid interface curvature [61]. If the current concentration c is lower than the equilibrium concentration c_{eq}, the solution rate is larger than the precipitation rate and the source term r_c is positive; otherwise, the source term r_c is negative. Note that the new crack region is assumed to be filled promptly with saturated salt solution.

Remark 1. The material coefficient α_s is introduced to fix the difference of the source term between Eq. (38) and the expression in Alkattan et al. [18]. In Eq. (38), the source term r_c has the unit mol m^{-3} s^{-1}, while the source term r_c in Alkattan et al. [18] has the unit mol m^{-2} s^{-1} representing the amount of salt migrating across the

solid/liquid interface. In this paper, the material coefficient α_s [unit: mm^{-1}], which is inversely proportional to the grain boundary thickness, converts the surface source term to the volumetric source term by assuming that the mass migration across the interface region is evenly distributed across the grain boundary region. This coefficient also includes the ratio between the actual grain boundary area and the homogenized grain boundary area.

Furthermore, the crack tip curvature may also influence the chemical potential of the solid phase and provide the driving force for diffusion-controlled crack healing. In the meantime, the equilibrium chemical concentration C_{eq} of the interfacial brine can be derived through the equality between the solid-phase chemical potential μ_{se} and the brine chemical potential μ at equilibrium status. At the room temperature, the chemical potential of the solid phase μ_{se} is a function of the pressure p and principle curvature $1/r$ (only one component for 2D):

$$\mu_{se} = f + p\Omega_v + \frac{\Omega_v \gamma_{sl}}{r} = \mu_0 + 2R\theta \ln \frac{C_{eq}}{C_0}, \tag{39}$$

where f is the free energy of the solid phase under atmospheric pressure, Ω_v is the molecular volume of the solid, γ_{sl} is the interfacial energy between solid and liquid phase, and μ_0 and C_0 are the reference chemical potential and concentration. The crack tip radius is positive for convex a solid interface. With the expression in Eq. (36) for chemical potential, the equilibrium concentration c_{eq} is defined such that the chemical potential of the solute in brine equals to that of the adjacent solid-phase μ_{se}. Therefore, the equilibrium concentration (c_{eq}) at crack tip can be written as an explicit function of the pressure p and principle curvature $1/r$ (2D):

$$c_{eq} = c_{eq}^0 \exp\left(\frac{p\Omega_v}{2RT} + \frac{\gamma_{sl}\Omega_v}{2rRT}\right) \approx c_{eq}^0 \left(1 + \frac{p\Omega_v}{2RT} + \frac{\gamma_{sl}\Omega_v}{2rRT}\right), \tag{40}$$

where c_{eq}^0 is the equilibrium concentration at atmosphere pressure and room temperature with a straight solid–liquid interface.

When using the phase-field model to predict the fracture behavior, it is usually assumed that the crack tip is sharp and the crack tip radius is zero when the length-scale parameter l_0 approaches zero. Therefore, it is impossible to compute the crack tip curvature numerically. To overcome this problem, a user-input crack tip radius is assigned to the crack tip region with the help of the Heaviside function $H(x)$ for 2-dimensional case:

$$r = \begin{cases} r_0, & l_0^3 \left\| \left(\nabla^{\boldsymbol{x}} \nabla^{\boldsymbol{x}} d_c - \nabla^2 d_c \boldsymbol{I}\right) \cdot \nabla^{\boldsymbol{x}} d_c \right\| \geq \text{tol.} \\ \infty, & \text{otherwise} \end{cases} \tag{41}$$

where tol is the tolerance to differentiate the crack tip region from the crack region. Note that the second-order gradient of the phase-field is difficult to compute in finite element method, since the gradient of the polynomial shape function is not continuous across the element edge. The effect of Eq. (41) in capturing the crack tip region is shown in Fig. 4, where the phase field d_c is computed by the penalty term with $\mathcal{H} = 0$ in Eq. (29). Fig. 4(a) and (b) show the phase field and crack tip indicator of a 'C' shape crack, while Fig. 4(c) and (d) show the phase field and crack tip indicator of two crossed cracks. The proposed criterion is effective in capturing the crack tip region even for a curved crack. Note that Eq. (41) can be only applied for high-order phase-field model. For second-order phase-field model, the second-order gradient has singular values, which will cause numerical issues when determining the crack tip region.

Combining Eqs. (5), (37), and (38), the final form of the diffusion equation can be written as:

$$\dot{c} - D_0 \nabla^{\boldsymbol{x}} \cdot \left(d_i \nabla^{\boldsymbol{x}} c\right) = d_i \left(d_c, d_{\mathrm{GB}}\right) \alpha_s k_s \left(c_{eq} - c\right), \tag{42}$$

where the equilibrium concentration c_{eq} depends on local pressure and solid–liquid interface curvature.

3.3. Constitutive relations for anisotropic phase field and crack healing

In this section, the anisotropic tensor $\mathbb{A}$ for the high-order phase field problem (29) is introduced. Furthermore, a crack propagation driving force $\mathcal{H}$ taking account of both cracking and healing is proposed.

In the high-order phase-field problem (29), the fourth-order anisotropic tensor $\mathbb{A}$ forms non-convex cleavage energy in the polar plot. For material with cubic symmetry, the anisotropic tensor $\mathbb{A}$ adopts the general form [62]:

$$\mathbb{A} = \mathbb{I} + \alpha_{apf}(\boldsymbol{A}_1 \otimes \boldsymbol{A}_1 + \boldsymbol{A}_2 \otimes \boldsymbol{A}_2) + \beta_{apf}\, \mathrm{sym}(\boldsymbol{A}_1 \otimes \boldsymbol{A}_2), \tag{43}$$

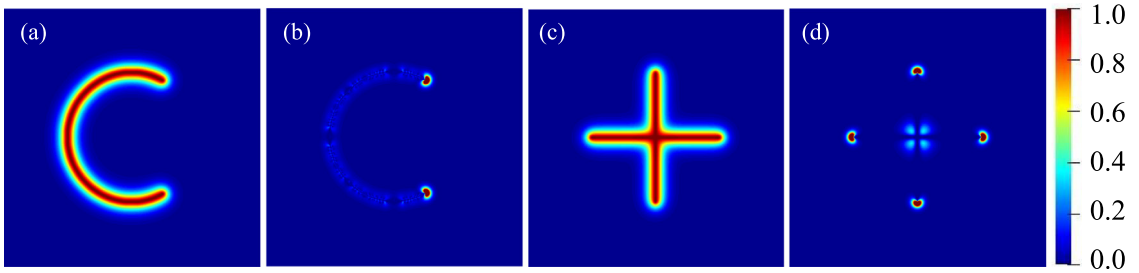

Fig. 4. Effectiveness of using Eq. (41) to detect the crack tip region. Both the phase field and the crack tip indicator are computed numerically with spectral basis functions. The crack region detection criteria takes the value $l_0^3 \left\| \left(\nabla^{\boldsymbol{x}} \nabla^{\boldsymbol{x}} d_c - \nabla^2 d_c \boldsymbol{I}\right) \cdot \nabla^{\boldsymbol{x}} d_c \right\|$. (a) Initial phase field distribution of curved crack using high-order phase-field model; (b) Crack tip determination criteria of curved crack; (c) Initial phase field distribution of intersecting crack using high-order phase-field model; (d) Crack tip determination criteria of intersecting crack.

where $\mathbb{I}$ is the fourth order identity tensor, α_{apf} and β_{apf} are material parameters penalizing the anisotropy, and $\boldsymbol{A}_1$ and $\boldsymbol{A}_2$ are second order anisotropic tensors determined by the preferential cleavage plane of rock salt. The phase-field problem reduces to an isotropic case if the coefficients α_{apf} and β_{apf} vanish. In order for the anisotropic tensor $\mathbb{A}$ to be positive definite, the following criteria shall be met:

$$\alpha_{apf} > -1, \quad |\beta_{apf}| < 2|1 + \alpha_{apf}| \tag{44}$$

Let $\boldsymbol{a}_1$ and $\boldsymbol{a}_2$ represent the normal directions of two perpendicular cleavage planes of single crystal rock salt which are determined by the initial orientation, then the second order anisotropic tensors $\boldsymbol{A}_1$ and $\boldsymbol{A}_2$ can be defined as:

$$\boldsymbol{A}_1 = \boldsymbol{a}_1 \otimes \boldsymbol{a}_1, \quad \boldsymbol{A}_2 = \boldsymbol{a}_2 \otimes \boldsymbol{a}_2. \tag{45}$$

In the typical phase-field based brittle fracture model, the driving force $\mathcal{H}$ is forced to be monotonically increasing by keeping its maximum historical value, since the crack healing process is not prevented by the thermodynamic laws. Herein, it is assumed that the healing process is activated when the total strain is volumetric compression by allowing the phase-field driving force to decrease. The phenomenological model for halite cleavage plane healing based on solution–precipitation kinetics is proposed in this paper, considering that the stiffness recovery rate becomes slower along with the healing process [28]:

$$\mathcal{H}_{n+1} = \max\left[\mathcal{H}_n - \alpha_h \mathcal{H}_n \langle -r_c \rangle V_m \Delta t,\ w_+^e\right]. \tag{46}$$

Here, w_0^p is the reference plastic work controlling the contribution of accumulated plastic work w^p on phase field evolution, and α_h is a non-dimensional coefficient indicating the percentage of contribution from precipitation to stiffness recovery.

Note that the crack healing is also possible when the crack is opening [6]. In this case, the healing process is accomplished through solution–precipitation in a thin water film coated on the crack wall. This process is much slower than the crack closure case when the crack region is filled with brine, and therefore is not considered in this model.

4. Numerical aspect on FFT-based method

The boundary value problem consists the following governing equations: balance of linear momentum equation Eq. (6), the energy balance equation Eq. (28), the phase field problem Eq. (29), and the diffusion equation Eq. (42). These coupled equations are solved in an operator-split manner by a collocation FFT-based solver to take advantage of its globally C^∞ continuous basis functions and more efficient computational cost.

The mechanical equation can be efficiently solved by the matrix-free conjugate gradient method [63,64], even though the equivalent stiffness matrix is non-symmetric. Balance of linear momentum (6) can be re-formulated in a periodic domain with the help of the Green's operator $\mathbb{G}$ independent of the reference material [65]:

$$\begin{cases} \mathbb{G} * \boldsymbol{\sigma} = \boldsymbol{0} & \text{in spatial domain} \\ \mathcal{F}^{-1}\left[\hat{\mathbb{G}} : \mathcal{F}(\boldsymbol{\sigma})\right] = \boldsymbol{0} & \text{in frequency domain.} \end{cases} \tag{47}$$

Here, the operator $*$ denotes convolution, which can be computed conveniently in the frequency domain. The Green's operator $\mathbb{G}$ used in this paper is independent of the reference material, which projects an arbitrary strain field to its compatible part. The major idea of the Newton–Krylov method is to use an iterative linear solver to solve the linearized form of Eq. (47), but instead of assembling the stiffness matrix, the convolution operation is performed utilizing FFT. Compared with the traditional fixed-point scheme, accelerated scheme, and the augmented Lagrangian scheme, the Newton–Krylov method generally exhibits better numerical efficiency. However, a major trade-off is that the Newton–Krylov method fails to converge when the spatial domain contains jump conditions such as a sharp contract of material properties. This issue can be alleviated numerically by replacing the sharp material contract with regularized interfacial representation via implicit function and introducing a residual stiffness for a completely damaged zone. Note that due to the periodic nature of the trigonometric basis functions and the numerical efficiency of the FFT-based method, the FFT-based method is frequently used for homogenization and concurrent multiscale modeling [66]. The numerical efficiency of the microscale simulation within the multiscale modeling can be improved by reducing the number of basis functions in FFT-based method [67], or using discrete harmonics based homogenization [68].

The temperature field is updated in a semi-implicit fashion using the FFT-based method [69]. The temperature field can be directly updated semi-implicitly when the thermal conductivity κ and specific heat C_v are homogeneous and temperature independent, where the temperature increasing rate $\dot{\theta}$ is approximated by first-order backward difference and the heat source is approximated by first-order Adams–Bashforth approximation. By taking the strain energy dissipation from the last converged step, the temperature field update at step $(n+1)$ can be performed in the frequency domain as:

$$\hat{\theta}_{n+1} = \frac{C_v \hat{\theta}_n + \hat{r}_\theta + \mathcal{F}\left[\boldsymbol{\sigma}_n : \dot{\boldsymbol{\varepsilon}}_n^p - 3\alpha K \theta_n \boldsymbol{I} : \dot{\boldsymbol{\varepsilon}}_n^e\right]}{C_v + \kappa \boldsymbol{k} \cdot \boldsymbol{k} \Delta t} \tag{48}$$

where $\boldsymbol{k}$ is the frequency vector, Δt is the time step increment, and $\hat{\cdot}$ denotes quantities in the frequency domain.

The continuum form of the high-order phase-field (29) defined in the periodic RVE can also be solved by the FFT-based spectral method. The gradient operator and Laplacian operator can be conveniently computed in the frequency domain, and the Gibbs effect can be alleviated utilizing the finite-difference based frequency vector. Assuming that the anisotropic tensor $\mathbb{A}$, the cleavage energy G_c, and length scale l_0 are piecewise constant and periodic, the continuous linear equation (29) can be discretized as:

$$\left(2\mathcal{H} + \frac{G_c}{l_0} + \frac{G_c l_0}{2}\mathcal{F}^{-1}\boldsymbol{k}\cdot\boldsymbol{k}\mathcal{F} + \frac{G_c l_0^3}{16}\mathbb{A} :: \mathcal{F}^{-1}\boldsymbol{k}\otimes\boldsymbol{k}\otimes\boldsymbol{k}\otimes\boldsymbol{k}\mathcal{F} + \beta_{ipf}\right) d_c = 2\mathcal{H} + \beta_{ipf}. \tag{49}$$

The stiffness matrix is not Hermitian unless the anisotropic tensor $\mathbb{A}$ is homogeneous, therefore the generalized minimal residual (GMRES) method is used to solve this equation. A modified driving force $\mathcal{H}$ based on Eq. (46) instead of a typical monotonically increasing driving force (30) is used to allow diffusion-controlled crack healing. Also, the initial defect region is enforced by the penalty method to avoid sharp material contrast, which leads to deteriorated convergence behavior of the mechanical equation (47).

The diffusion equation (42) can be discretized by estimating the gradient operator in the frequency domain:

$$\begin{cases} \left[1 + \alpha_s k_s \Delta t d_i - \bar{\lambda}\mathcal{F}^{-1}(i\boldsymbol{k})\cdot(i\boldsymbol{k})\mathcal{F} - \mathcal{F}^{-1}(i\boldsymbol{k})\cdot\left(\mathcal{F}\tilde{\lambda}(\boldsymbol{x})\mathcal{F}^{-1}(i\boldsymbol{k})\mathcal{F}\right)\right] c_{n+1} = c_n + \alpha_s k_s \Delta t d_i c_{eq} \\ \lambda(\boldsymbol{x}) = \bar{\lambda} + \tilde{\lambda}(\boldsymbol{x}) = d_i D_0 \Delta t. \end{cases} \tag{50}$$

The stiffness matrix is Hermitian, so the conjugate gradient (CG) method is used to solve this equation. The equilibrium concentration c_{eq} depends on the pressure field and phase-field of last converged time step. The diffusion equation is more involved to be solved by the FFT-based spectral method in two aspects. First, the material parameters are continuously varying making it impossible to update the concentration field semi-implicitly. Although the varying diffusivity can be split into a volume average part and a perturbation part [69], a fully implicit scheme is adopted considering that the solution–diffusion–precipitation process requires a long time step [42]. Second, the large diffusivity contrast between the interfacial region and the bulk region is highly heterogeneous and will introduce numerical issues. This problem can be alleviated by selecting a proper diffusivity residual for the bulk region.

The coupled thermo-chemo-mechanical-phase field equations are solved in a staggered iterative scheme. The detailed algorithm is presented in Algorithm 1. For the mechanical problem, either average stress components or

strain components are provided at the start of each time step, and the stress/strain components are mutually exclusive. For example, the following average stress/strain could serve as the boundary condition for displacement-controlled uniaxial tension:

$$\bar{\boldsymbol{\sigma}} = \begin{bmatrix} * & 0 & 0 \\ 0 & 0 & 0 \\ 0 & 0 & 0 \end{bmatrix}, \quad \bar{\boldsymbol{\varepsilon}} = \begin{bmatrix} \bar{\varepsilon}_{11} & * & * \\ * & * & * \\ * & * & * \end{bmatrix}. \tag{51}$$

Two Newton iterations are utilized to solve this problem. The outer iteration updates the average strain components based on the strain boundary condition and the deviation between average stress and stress boundary condition. The inner iteration solves the Lippmann–Schwinger equation with the most updated strain components. Then, the thermal equation, the diffusion equation, and the phase-field equation are solved successively. The internal variables and the equilibrium concentration c_{eq} are updated at the end of each time step.

Algorithm 1: FFT-based thermal–mechanical phase field problem.

for $n \leftarrow 1$ **to** nstep **do**
  if *Strain boundary condition* **then** $\Delta\bar{\boldsymbol{\varepsilon}} = \Delta\bar{\boldsymbol{\varepsilon}}_{BC}$;
  else $\Delta\bar{\boldsymbol{\varepsilon}} = \bar{\boldsymbol{C}}_n^{-1} \Delta\bar{\boldsymbol{\sigma}}_{BC}$;
  while true **do**
    $\boldsymbol{\varepsilon}_{n+1} = \boldsymbol{\varepsilon}_{n+1} + \Delta\bar{\boldsymbol{\varepsilon}}$;
    solve for $\Delta\tilde{\boldsymbol{\varepsilon}}$: $\mathbb{G} * (\boldsymbol{C}_n : \Delta\tilde{\boldsymbol{\varepsilon}}) = -\mathbb{G} * (\boldsymbol{C}_n : \Delta\bar{\boldsymbol{\varepsilon}})$;
    update $\boldsymbol{\varepsilon}_{n+1}$: $\boldsymbol{\varepsilon}_{n+1} = \boldsymbol{\varepsilon}_{n+1} + \Delta\tilde{\boldsymbol{\varepsilon}}$;
    while $R >$ tol. **do**
      $\Delta\boldsymbol{\varepsilon} = \boldsymbol{\varepsilon}_{n+1} - \boldsymbol{\varepsilon}_n - \alpha(\theta_n - \theta_{n-1})\boldsymbol{I} - \Delta\boldsymbol{\varepsilon}^c$
      update $\boldsymbol{\sigma}_{n+1}$: $\boldsymbol{\sigma}_{n+1} = f\,(\Delta\boldsymbol{\varepsilon}, \boldsymbol{\sigma}_n, d_c, \text{history})$;
      solve for $\Delta\tilde{\boldsymbol{\varepsilon}}$: $\mathbb{G} * (\boldsymbol{C}_{n+1} : \Delta\tilde{\boldsymbol{\varepsilon}}) = -\mathbb{G} * \boldsymbol{\sigma}_{n+1}$;
      update $\boldsymbol{\varepsilon}_{n+1}$: $\boldsymbol{\varepsilon}_{n+1} = \boldsymbol{\varepsilon}_{n+1} + \Delta\tilde{\boldsymbol{\varepsilon}}$;
      update residual: $R = \|\Delta\tilde{\boldsymbol{\varepsilon}}\|$;
    end
    $\bar{\boldsymbol{\sigma}} = \langle\boldsymbol{\sigma}_{n+1}\rangle$;
    if $\frac{\|\bar{\boldsymbol{\sigma}} - \boldsymbol{\sigma}_{BC}\|}{\|\bar{\boldsymbol{\sigma}}\|} <$ tol. **then** break;
    update $\bar{\boldsymbol{C}}_{n+1}$ using equation;
    update $\Delta\bar{\boldsymbol{\varepsilon}}$: $\Delta\bar{\boldsymbol{\varepsilon}} = -\bar{\boldsymbol{C}}_{n+1}^{-1} (\bar{\boldsymbol{\sigma}} - \boldsymbol{\sigma}_{BC})$;
  end
  Update temperature θ by solving Eq. (48) ;
  Update phase field d_c by solving equation Eq. (49) ;
  Update chemical concentration c and chemical source r_c by solving equation Eq. (50) ;
  Update internal variables $\tilde{\tau}$ from step $n+1$ to step n ;
  compute c_{eq} from Eq. (40), $\mathcal{H}$ from Eq. (46), $\Delta\boldsymbol{\varepsilon}^c$ from Eq. (5) ;
end

5. Examples

In this section, numerical examples are presented to demonstrate the capability of the proposed numerical framework in capturing the coupled physical process in rock salt. In particular, the interplay among crystal plasticity, strongly anisotropic cracking, solution–precipitation, and crack healing is, for the first time, replicated explicitly in numerical simulations. We first calibrate the material model for crystal plasticity with data available from the literature. Then we introduce physics-based material parameters for the phase-field fracture, thermal diffusion and chemical transport. Then, a polycrystalline RVE creep simulation with constant stress boundary condition is performed to illustrate the solution–precipitation creep within the interfacial region. A polycrystalline RVE simulation with monotonically increasing loading is performed to capture the competition between intergranular and intragranular fracture in polycrystalline rock salt. Finally, a cyclic loading numerical example is used to demonstrate the capability of the proposed crack healing model in capturing the diffusion-controlled crack healing.

Table 1
Material properties for crystal plasticity.

Parameters	Description	Value	Unit	Reference
E	Elastic modulus	38.0	GPa	Na and Sun [9]
ν	Poisson's ratio	0.25	–	Na and Sun [9]
n	Rate sensitivity exponent	15.0	–	–
$\bar{\gamma}$	Rate normalization factor	1.0×10^{-10}	s^{-1}	–
τ_y	Initial yield stress	0.5	MPa	–
τ_v	Saturation stress	10.0	MPa	–
m	Hardening exponent	1.0	–	–
h_0	Initial hardening rate	30.0	MPa	–

Table 2
Material properties for strongly anisotropic phase field.

Parameters	Description	Value	Unit	Reference
G_c	Cleavage energy	1.15	$J\,m^2$	Na and Sun [9]
l_0	Length scale	1.0×10^{-5}	m	Na and Sun [9]
β_{ipf}	Initial phase field penalty	1000.0	–	–
α_{apf}	Anisotropy factor	1.2	–	–
r_0	Crack tip radius	0.5–5	μm	Koelemeijer et al. [6]
β_{apf}	Anisotropy factor	1000.0	–	–

Table 3
Material properties for thermal problem.

Parameters	Description	Value	Unit	Reference
α	Thermal expansion coefficient	11.0×10^{-6}	K^{-1}	Na and Sun [9]
c_v	Specific heat	2.0×10^6	$J\,m^{-3}\,K^{-1}$	Na and Sun [9]
κ	Thermal conductivity	2.0	$W\,m^{-1}\,K^{-1}$	Na and Sun [9]

5.1. Simulation setup and material model calibrations

Rock salt single crystal exhibits a face-centered-cubic (FCC) structure. Along with the typical $\{111\}\langle 1\bar{1}0\rangle$ slip systems, two other slip systems are also observed including $\{110\}\langle 1\bar{1}0\rangle$ and $\{100\}\langle 1\bar{1}0\rangle$. The $\{110\}\langle 1\bar{1}0\rangle$ slip system has the lowest critical resolved stress at room temperature [70], while the other two slip systems have 6 times larger critical resolved shear stress than $\{110\}\langle 1\bar{1}0\rangle$ [20,21]. Note that the $\{110\}\langle 1\bar{1}0\rangle$ slip system provides only two independent variants, while five independent variants are required to accommodate an arbitrary plastic strain. In this paper, only the $\{110\}\langle 1\bar{1}0\rangle$ slip system is considered to be consistent with our previous work [9].

The single crystal uniaxial compression experiments from Carter and Heard [70] are used to calibrate the crystal plasticity parameters. The elastic constants of single crystal rock salt are from Carter and Norton [71]. Although rock salt has a cubic symmetry crystal structure, its elastic anisotropy factor is almost one, so isotropic elastic constants are used. Since the Voce model Eqs. (33)–(35) are independent of temperature, only room temperature stress–strain curves are used with three different strain rates. A single crystal RVE is loaded in the [001] direction with uniaxial compression boundary conditions. The calibrated material parameters for crystal plasticity are shown in Table 1. The comparison between the experiment and the simulation is shown in Fig. 5.

The material parameters for the phase-field fracture model are shown in Table 2. The cleavage energy G_c is taken from our previous paper [9], and other parameters are adjusted such that the strongly anisotropic cleavage behaviors observed experimentally are satisfied. Typical crack tip radius and crack opening angle are taken from Koelemeijer et al. [6]. The preferential cleavage plane is $\{100\}$.

The thermal parameters [9] and the diffusional parameters [18] are shown in Tables 3 and 4, respectively. The crack healing coefficient α_h is manually adjusted to qualitatively meet the experimental crack healing rate [5], although the experiment is designed for opening crack adsorbed with thin brine film which makes quantitative comparison impossible. Simplifications are adopted such that the interfacial region has the same thermal conductivity and thermal expansion as the grain bulk region. Also, it is assumed that the thickness of the brine film is much

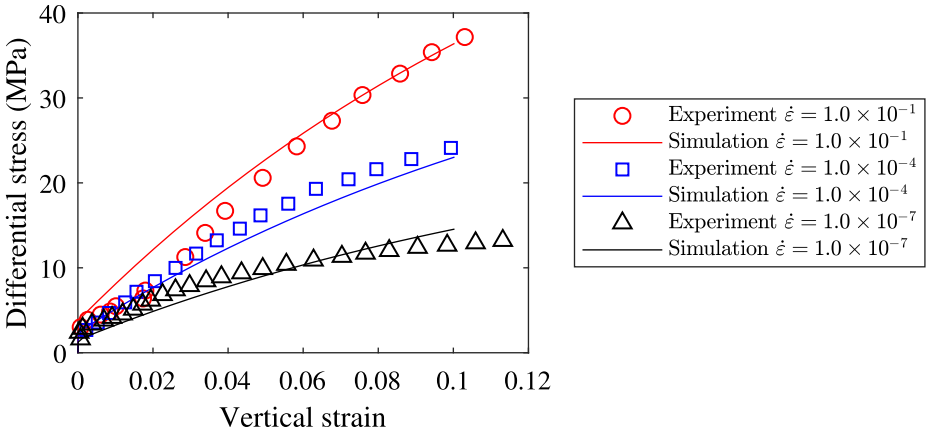

Fig. 5. Confined compression stress–strain response with different strain rates at room temperature [70].

Table 4
Material properties for diffusion.

Parameters	Description	Value	Unit	Reference
D_0	Diffusion coefficient	2.2×10^{-3}	$m^2\,s^{-1}$	Alkattan et al. [18]
k_s	solution–precipitation coefficient	5.0×10^{-1}	$m\,s^{-1}$	Alkattan et al. [18]
γ_{sl}	Solid–liquid interfacial energy	0.129	$J\,m^{-2}$	Houben et al. [5]
Ω_v	Molecular volume of solid NaCl	2.7×10^{-5}	$m^3\,mol^{-1}$	Koelemeijer et al. [6]
R	Ideal gas constant	8.314	$J\,mol^{-1}\,K^{-1}$	Koelemeijer et al. [6]
α_s	Grain boundary thickness coefficient	1000.0	m^{-1}	–
α_h	Crack healing coefficient	10.0	–	–
c_0^{eq}	Equilibrium concentration	5416.0	$mol\,m^{-3}$	Alkattan et al. [18]

larger than several hundred nanometers such that the diffusion coefficient D_0 and solubility c_{eq} of the macroscale brine are representative.

5.2. Long-term creeping due to solution–precipitation

In this numerical example, a series of creep simulations are performed to illustrate the solution–precipitation creep observed in polycrystalline rock salt [15]. The numerical set-up is shown in Fig. 6(a). A four-grain RVE is constructed with 1 mm edge length. The initial orientations of the grains are denoted in Fig. 6(a), with [001] axis perpendicular to the xy plane. Constant average stress rate is enforced during the loading period until the destinate stress is reached, and then constant stress boundary condition is enforced during the creep deformation period.

Grain boundary layer with 0.05 mm thickness is introduced between each pair of grains, and initial grain boundary indicator d_{GB} is assigned to the grain boundary region. Crystal plasticity constitutive relation is assigned to the grain boundary region, and the initial orientation inherits from the neighboring grains. In the current model, grain boundary thickness is also a key material parameter. The grain boundary thickness in numerical simulation should be chosen as a compromise between the real grain boundary, where solution–diffusion–precipitation occurs, and the computational cost. The solution–precipitation creep rate increases as the grain boundary thickness increases. A constant grain boundary thickness should be used for different RVEs to reveal size effect instead of using an arbitrary fraction of the RVE edge length.

The triple junctions of the grain boundary region also require proper treatment regarding the grain boundary normal and the solution–precipitation strain mode. Here, the solution–precipitation creep deformation $\dot{\boldsymbol{e}}$ equals to zero at the triple junctions, but the initial phase field is enforced as 1 for compensation. Otherwise, the triple junctions become rigid inclusions as creep deformation increases.

In this paper, only solution–precipitation creep is considered instead of the competition between dislocation creep and solution–precipitation creep, since the hardening variable $\tilde{\tau}$ is monotonically increasing in the Voce type crystal

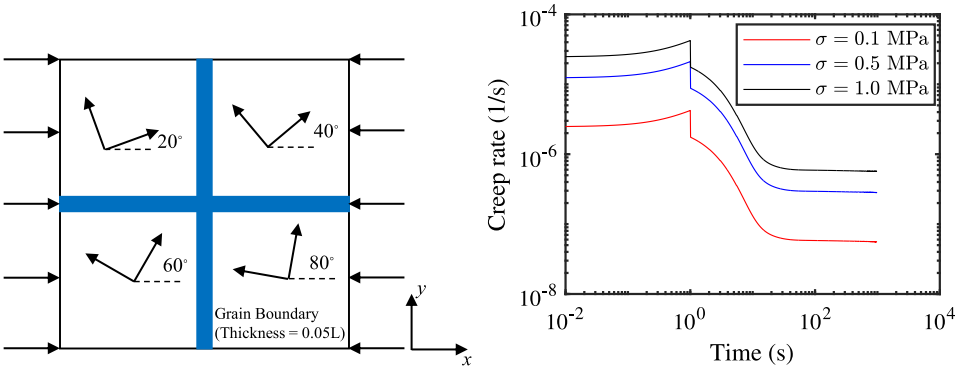

(a) The set-up for creep test **(b)** Creep rate evolution

Fig. 6. Analysis of creep loading effect on solution–precipitation creep rate: (a) The numerical set-up for the creep simulation; (b) Creep rate evolution for each creep loading condition.

plasticity model Eqs. (33)–(35). The dislocation creep can be incorporated by introducing a dislocation annihilation mechanism to allow decreasing hardening variables.

Fig. 6(b) shows the creep rate evolution during the creep loading under different stress level. Three constant stress levels are tested: 0.1 MPa, 0.5 MPa, 1.0 MPa. During the constant stress-rate loading period, a monotonically increasing strain rate is observed which represents the transition from the elastic region to the plastic region. In the constant stress period, the strain rate gradually decreases due to the monotonically increasing hardening variable. Then, the creep strain rate reaches a constant value which depends on the stress level. It is also observed that the strain rate constant $n = 1$, which is consistent with the solution–precipitation creep experiment [15].

Fig. 7 shows the evolution of grain boundary brine concentration (a–c), longitudinal strain (d–f), and transverse strain (g–i) for the $\sigma = 1.0$ MPa case. It is observed that as time increases, the grain boundary brine concentration almost remains constant. A concentration gradient exists along the grain boundary, where the high concentration region corresponds to the grain boundary region with higher grain boundary normal compression. Concentration flux normal to the grain boundary is almost negligible, although slight concentration increasing is observed at the grain bulk adjacent to the grain boundary. On the other hand, creep deformation is observed in the grain boundary region as time increases. A compressive grain-boundary-normal strain ε_{xx} is observed in the vertical grain boundary since the grain boundary pressure p is much higher than the horizontal grain boundary where tensile grain-boundary-normal strain ε_{yy} is observed. It is also observed that the compressive strain ε_{xx} in the vertical grain boundary region approximately equals the tensile strain ε_{yy} in the horizontal grain boundary region, indicating that the solution–precipitation model is mass conservative assuming that density is constant. Note that the strain values at the triple junctions have large perturbations, since four grains with different orientations interact with each other. The stiffness of the triple junction is reduced by imposing unit initial phase field d_c in this region.

5.3. Anisotropic cracking

The third example is designed to illustrate the anisotropic crack initiation and propagation in polycrystalline rock salt and the competition among intergranular and intragranular fracture, and plastic deformation.

A 2D polycrystalline RVE with 40 grains is generated by Neper [72], and the RVE is equally divided into 399×399 grid points, as shown in Fig. 8(a). The RVE edge length is 1 mm, and the average grain size is 0.2 mm. Random initial orientations are assigned to each grain with the [001] axis perpendicular to the xy plane, such that the cleavage planes are also perpendicular to the xy plane. The fracture energy G_c of the material point within the bulk region is 1.15 J m^2, and the preferential fracture plane is {001}. Reduced fracture energy (1.0 J m^2) is assigned to the grain boundary region, and the grain boundary is assumed to be isotropic in crack propagation. Small strain crystal plasticity model is applied to both the grain interior region and the grain boundary region. The grain boundary layer thickness approximately equals to $0.014L$, where L represents the RVE edge length. The deformation process is

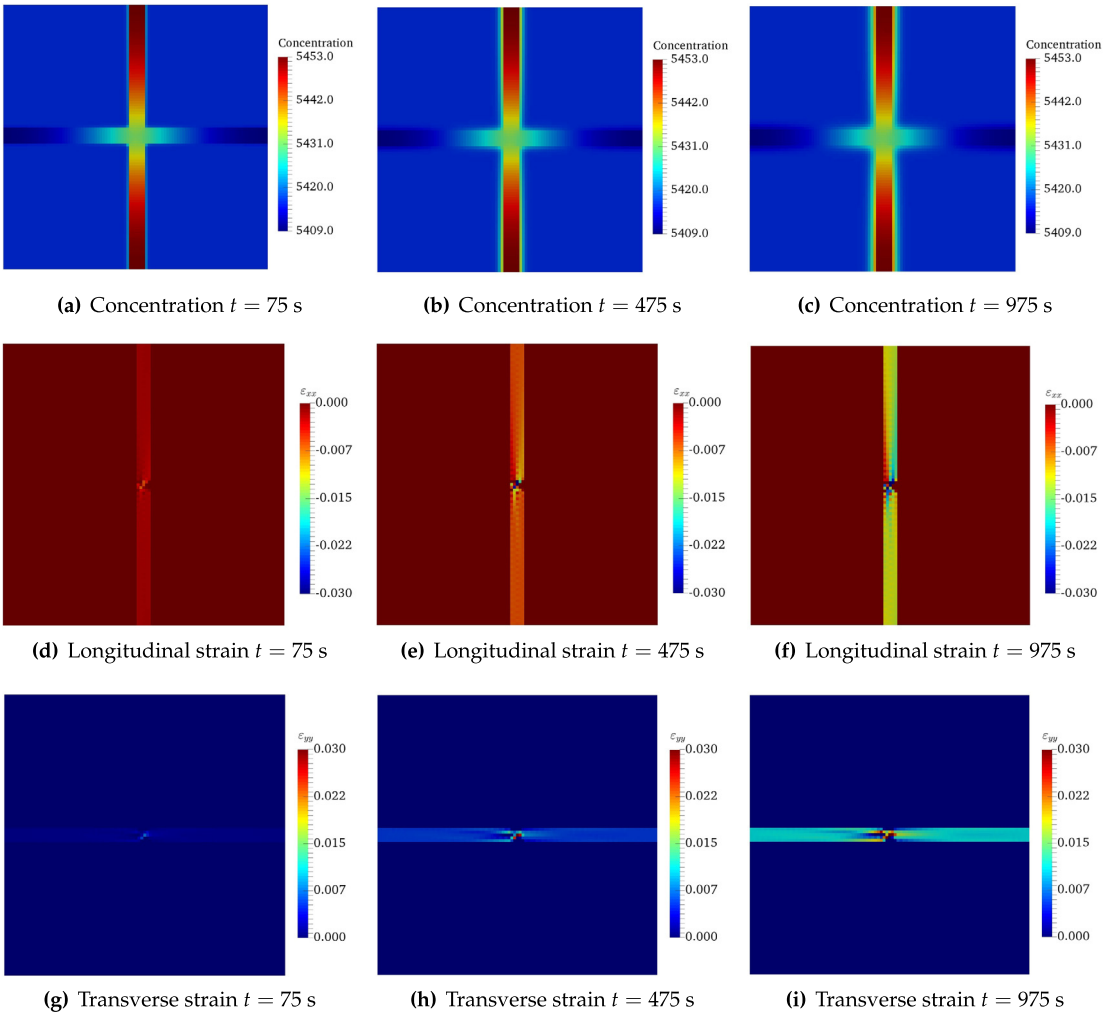

(a) Concentration $t = 75$ s **(b)** Concentration $t = 475$ s **(c)** Concentration $t = 975$ s

(d) Longitudinal strain $t = 75$ s **(e)** Longitudinal strain $t = 475$ s **(f)** Longitudinal strain $t = 975$ s

(g) Transverse strain $t = 75$ s **(h)** Transverse strain $t = 475$ s **(i)** Transverse strain $t = 975$ s

Fig. 7. Brine concentration and strain distribution at different creep stages for the $\sigma = 1$ MPa simulation in Fig. 6: (a–c) Evolution of grain boundary brine concentration [unit: mol m^{-3}]; (d–f) Evolution of strain in the loading direction ε_{xx}; (g–i) Evolution of strain in the transverse direction ε_{yy}.

assumed to be isothermal at room temperature, which is reasonable considering that the specimen size is relatively small.

Pure shear average strain is enforced as the boundary condition, with a constant average strain rate $\dot{\gamma} = 1.0 \times 10^{-4}\,\mathrm{s}^{-1}$:

$$\boldsymbol{\varepsilon} = \begin{bmatrix} \gamma & 0.0 \\ 0.0 & -\gamma \end{bmatrix}. \tag{52}$$

Fig. 8(b) shows the homogenized stress–strain response in the axial direction. It is observed that the fracture process of polycrystal rock salt is more ductile compared with corresponding single crystal results [9]. One major reason is that the grain boundary region and intergranular anisotropy prevent the crack from propagating through the specimen, as shown in Fig. 9(a–c). It is observed that as external loading increases, both intragranular crack and intergranular crack initiate and gradually form a network within the specimen.

The Von-Mises stress distributions at different loading stages are shown in Fig. 9(d–f). As expected, stress concentration is observed at the crack tip and the grain boundary regions. The Gibbs effect is also observed mainly for two reasons: (1) regular frequency vector is used instead for solving the mechanical problem of the finite difference based frequency vector; (2) large material stiffness contrast exists within the interfacial region.

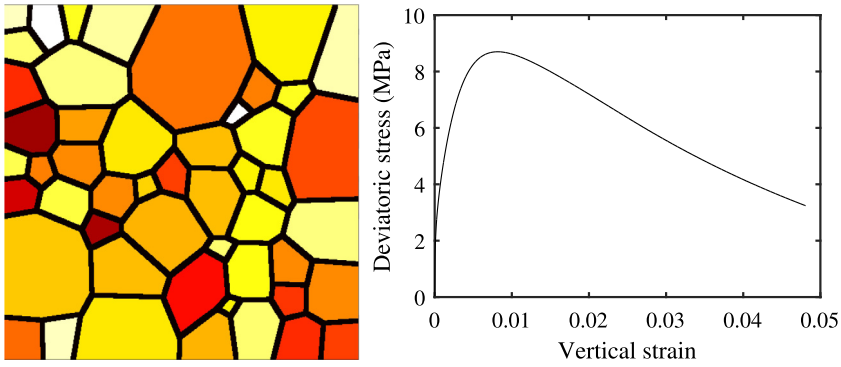

(a) Initial configuration of polycrystal RVE **(b)** Homogenized stress-strain curve

Fig. 8. Analysis of crack initiation and propagation in polycrystalline rock salt: (a) Initial configuration of polycrystal RVE and grain boundary. The RVE edge length L is 1 mm, and the grain boundary thickness is $l = 0.014L$, the initial orientation is random with [001] axis perpendicular to the xy plane. (b) Homogenized stress–strain curve.

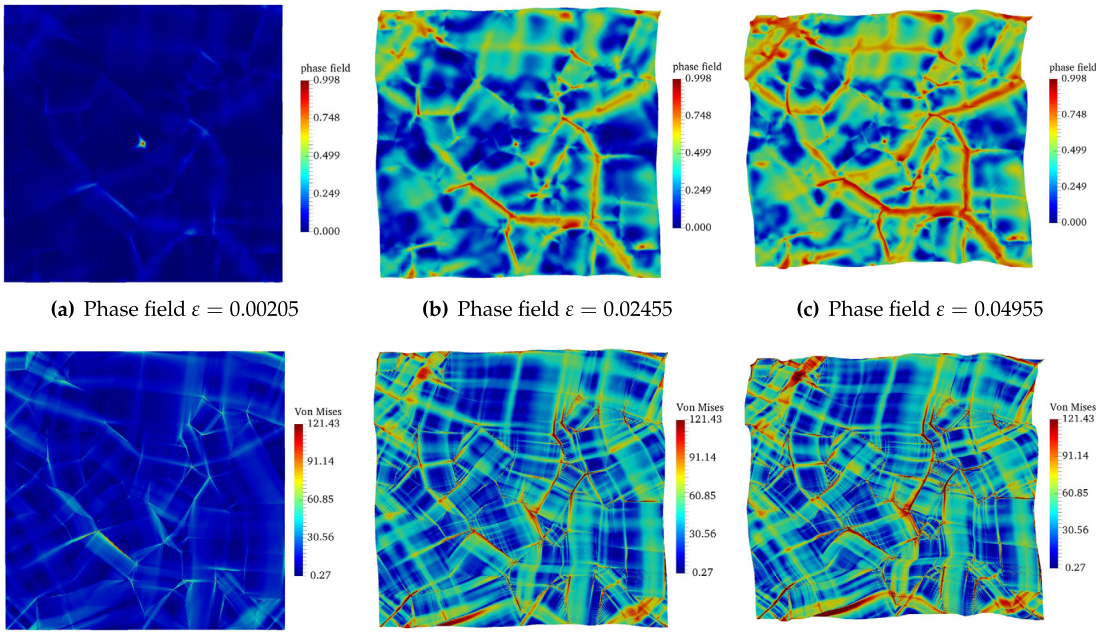

(a) Phase field $\varepsilon = 0.00205$ **(b)** Phase field $\varepsilon = 0.02455$ **(c)** Phase field $\varepsilon = 0.04955$

(d) Von Mises stress $\varepsilon = 0.00205$ **(e)** Von Mises stress $\varepsilon = 0.02455$ **(f)** Von Mises stress $\varepsilon = 0.04955$

Fig. 9. Phase field and Von Mises stress distribution within the polycrystal specimen at different load stages: (a–c) Phase field; (d–f) Von Mises stress ([unit: MPa]).

5.4. Chemical-diffusion-controlled crack healing

In the last example, diffusion-controlled crack healing is simulated through a prescribed loading–unloading–reloading strain path. A two-dimensional single-crystal RVE is divided into 399^2 grid points, and the edge length of the specimen is 1 mm by 1 mm. A circular flaw with 0.1 mm radius is introduced in the center of the specimen for crack initiation. The initial Euler angle is $(0°, 0°, 0°)$ in Bunge notation, such that the [100] axis is parallel to the loading direction. The loading–unloading–reloading strain path is shown in Fig. 10(a). A uniaxial tension boundary condition is conducted with a constant strain rate.

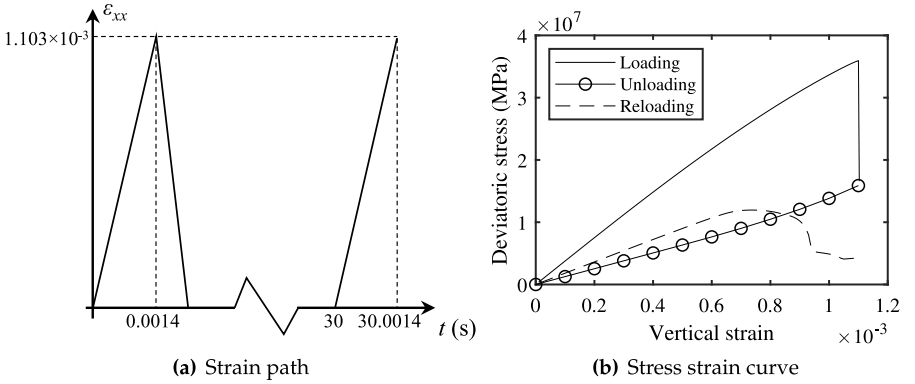

Fig. 10. Strain path and stress–strain curve of the crack healing simulation. (a) Strain path of the loading–unloading–reloading process. (b) Uniaxial stress–strain curve during the loading–unloading–reloading process. The RVE holds for a while with no external loading between the unloading process and the reloading process to provide enough time for crack healing.

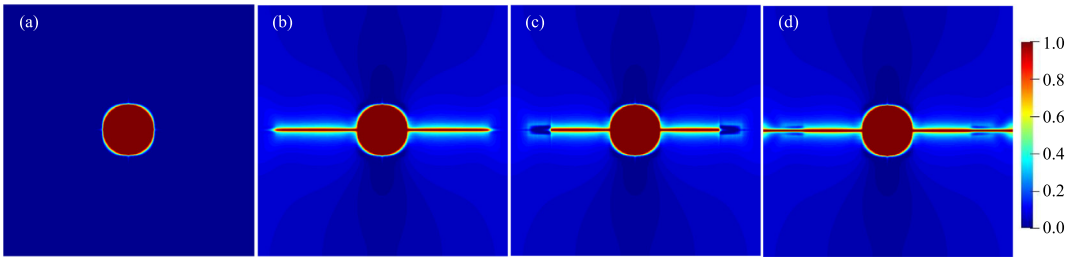

Fig. 11. Phase field evolution during the loading–unloading–reloading process. (a) Initial phase-field representing the initial circular flaw with 0.1 mm radius; (b) Fracture phase-field distribution after the loading and unloading process; (c) Crack healing after the stress-free holding process; (d) Crack propagation continues to penetrate the specimen after the reloading process.

In this section, the linear elastic constitutive relation is used instead of crystal plasticity for several reasons. First, creeping deformation during the healing process due to the residual stress can be avoided, such that the crack healing simulation could be more comparable to the experiment [5]. Also, the focus of this section is to demonstrate the effectiveness of the precipitation, diffusion, and crack healing model, and to determine whether crack healing in rock salt is diffusion-controlled or precipitation controlled. Note that the usage of elastic constitutive relation is solely for illustration convenience without losing generality.

The homogenized stress–strain response of the loading–unloading–reloading process is shown in Fig. 10(b). Reduced stress due to crack propagation is observed after the external loading reaches a critical point, and unloading boundary condition is initiated before the crack propagates through the specimen. This is possible for the staggered coupling scheme, where crack initiation and propagation are delayed compared with the corresponding monolithic coupling scheme. After the unloading process, the specimen is held at stress-free status for 300 s which is long enough for diffusion induced crack healing. Stiffness recovery is observed during the reloading process.

The evolution of the phase field during the loading–unloading–reloading process is shown in Fig. 11. The initial circular flaw with 0.1 mm radius is prescribed by the initial phase field, as shown in Fig. 11(a), to provide crack initiation spot. The fracture phase-field distributions after the loading process, the stress-free holding process, and the reloading process are shown in Fig. 11(b), (c), and (d), respectively. The crack does not penetrate through the specimen after the unloading process, as shown in Fig. 11(b). Crack healing is observed after the stress-free holding process as shown in Fig. 11(c), which explains the stiffness recovery observed in the homogenized stress–strain response in Fig. 10(b). During the reloading process, the crack continues to propagate along the original path when the external loading reaches a critical point.

The chemical concentration distributions corresponding to the time step described in Fig. 11(a–d) are shown in Fig. 12(a–d), respectively. The initial chemical concentration (Fig. 11(a)) is homogeneous and equals to the

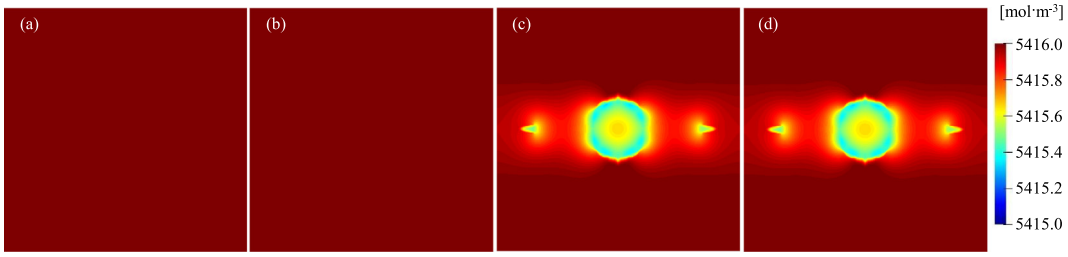

Fig. 12. Chemical concentration distribution during the loading–unloading–reloading process. (a) Homogeneous initial chemical concentration equals to the equilibrium concentration c_{eq} at stress free status; (b) Chemical concentration after the loading and unloading process corresponding to Fig. 11(b); (c) Chemical concentration distribution after the stress-free holding process corresponding to Fig. 11(c); (d) Chemical concentration after the reloading process corresponding to Fig. 11(d).

equilibrium chemical concentration at stress-free states. After the loading and unloading process, the chemical concentration remains unchanged, since the time is very short and both solution–precipitation and diffusion are time dependent. After holding the sample at stress-free states for 300 s which is long enough for solution–precipitation and diffusion to occur, the precipitation is observed within the crack tip region and the initial flaw region, as shown in Fig. 12(c). This precipitation causes the crack healing observed in Fig. 11(c) and the stiffness recovery observed in Fig. 10(b).

6. Conclusions

A mathematical framework is proposed to simulate the long-term creep, fracture and healing coupling process in rock salt under a variety of thermal, mechanical and chemical conditions. An FFT-based method is employed to solve the coupled equations in a staggered scheme. By leveraging the numerical efficiency and globally $\mathcal{C}^{\infty}$ continuous basis function, the strongly anisotropic crack growth and healing are simulated. Our numerical examples demonstrate that the proposed model is capable of replicating the multi-physical behaviors observed in rock salt, including solution–precipitation creep, strongly anisotropic cracking, and diffusion–controlled crack healing with stiffness restoration.

Declaration of competing interest

The authors declare that they have no known competing financial interests or personal relationships that could have appeared to influence the work reported in this paper.

Acknowledgments

This research is supported by the Nuclear Energy University program from the Department of Energy, United States of America under grant contract DE-NE0008534, the Earth Materials and Processes program from the US Army Research Office under grant contract W911NF-18-2-0306, the Dynamic Materials and Interactions Program from the Air Force Office of Scientific Research, United States of America under grant contracts FA9550-17-1-0169 and FA9550-19-1-0318, the Mechanics of Materials and Structures program at National Science Foundation, United States of America under grant contract CMMI-1462760 and the National Science Foundation, United States of America CAREER grant CMMI-1846875, as well as the Office of Advanced Cyberinfrastructure at National Science Foundation, United States of America under grant contract CSE-1940203. These supports are gratefully acknowledged. The views and conclusions contained in this document are those of the authors, and should not be interpreted as representing the official policies, either expressed or implied, of the sponsors, including the U.S. Government. The U.S. Government is authorized to reproduce and distribute reprints for government purposes notwithstanding any copyright notation herein.

References

[1] Kristopher L. Kuhlman, Historic testing relevant to disposal of heat-generating waste in salt, Technical Report, Sandia National Lab.(SNL-NM), Albuquerque, NM (United States), 2013.

[2] Laura Blanco Martin, Jonny Rutqvist, Jens T. Birkholzer, Long-term modeling of the thermal–hydraulic–mechanical response of a generic salt repository for heat-generating nuclear waste, Eng. Geol. 193 (2015) 198–211.

[3] Soheil Ghanbarzadeh, Marc A. Hesse, Maša Prodanović, James E Gardner, Deformation-assisted fluid percolation in rock salt, Science 350 (6264) (2015) 1069–1072.

[4] Cheng Zhu, Ahmad Pouya, Chloé Arson, Micro-macro analysis and phenomenological modelling of salt viscous damage and application to salt caverns, Rock Mech. Rock Eng. 48 (6) (2015) 2567–2580.

[5] M.E. Houben, A. ten Hove, C.J. Peach, C.J. Spiers, Crack healing in rocksalt via diffusion in adsorbed aqueous films: Microphysical modelling versus experiments, Phys. Chem. Earth A/B/C 64 (2013) 95–104.

[6] Paula J. Koelemeijer, Colin J. Peach, Christopher J. Spiers, Surface diffusivity of cleaved NaCl crystals as a function of humidity: impedance spectroscopy measurements and implications for crack healing in rock salt, J. Geophys. Res. Solid Earth 117 (B1) (2012).

[7] R.C.M.W Franssen, C.J. Spiers, Deformation of polycrystalline salt in compression and in shear at 250–350°C, Geol. Soc. Lond. Spec. Publ. 54 (1) (1990) 201–213.

[8] Hugh C. Heard, Steady-state flow in polycrystalline halite at pressure of 2 kilobars, Flow Fract. Rocks 16 (1972) 191–209.

[9] SeonHong Na, WaiChing Sun, Computational thermomechanics of crystalline rock, Part I: A combined multi-phase-field/crystal plasticity approach for single crystal simulations, Comput. Methods Appl. Mech. Engrg. 338 (2018) 657–691.

[10] Ahmad Pouya, Cheng Zhu, Chloé Arson, Micro–macro approach of salt viscous fatigue under cyclic loading, Mech. Mater. 93 (2016) 13–31.

[11] Eric C. Bryant, WaiChing Sun, A micromorphically regularized Cam-clay model for capturing size-dependent anisotropy of geomaterials, Comput. Methods Appl. Mech. Engrg. 354 (2019) 56–95.

[12] Shi-Yuan Li, Janos L. Urai, Rheology of rock salt for salt tectonics modeling, Pet. Sci. 13 (4) (2016) 712–724.

[13] Vladislav Kruzhanov, B. Stöckhert, On the kinetics of elementary processes of pressure solution, Pure Appl. Geophys. 152 (4) (1998) 667–683.

[14] Stephen H. Hickman, Brian Evans, Kinetics of pressure solution at halite-silica interfaces and intergranular clay films, J. Geophys. Res. Solid Earth 100 (B7) (1995) 13113–13132.

[15] Jacques Schott, Oleg S. Pokrovsky, Eric H. Oelkers, The link between mineral dissolution/precipitation kinetics and solution chemistry, Rev. Miner. Geochem. 70 (1) (2009) 207–258.

[16] Reinier van Noort, Hendrica J.M. Visser, Christopher J. Spiers, Influence of grain boundary structure on dissolution controlled pressure solution and retarding effects of grain boundary healing, J. Geophys. Res.: Solid Earth 113 (B3) (2008).

[17] R. Van Noort, C.J. Spiers, C.J. Peach, Effects of orientation on the diffusive properties of fluid-filled grain boundaries during pressure solution, Phys. Chem. Miner. 34 (2) (2007) 95–112.

[18] Marwan Alkattan, Eric H Oelkers, Jean-Louis Dandurand, Jacques Schott, Experimental studies of halite dissolution kinetics, 1 the effect of saturation state and the presence of trace metals, Chem. Geol. 137 (3–4) (1997) 201–219.

[19] Guillaume Desbois, Janos L. Urai, Johannes H.P. de Bresser, Fluid distribution in grain boundaries of natural fine-grained rock salt deformed at low differential stress (Qom Kuh salt fountain, central Iran): Implications for rheology and transport properties, J. Struct. Geol. 43 (2012) 128–143.

[20] H.R. Wenk, G. Canova, A. Molinari, H. Mecking, Texture development in halite: comparison of Taylor model and self-consistent theory, Acta Metall. 37 (7) (1989) 2017–2029.

[21] Ricardo A Lebensohn, Paul R Dawson, Hartmut M Kern, Hans-Rudolf Wenk, Heterogeneous deformation and texture development in halite polycrystals: comparison of different modeling approaches and experimental data, Tectonophysics 370 (1–4) (2003) 287–311.

[22] S. Olivella, J. Carrera, A. Gens, E.E. Alonso, Nonisothermal multiphase flow of brine and gas through saline media, Transp. Porous Media 15 (3) (1994) 271–293.

[23] Allan F. Bower, Emeric Wininger, A two-dimensional finite element method for simulating the constitutive response and microstructure of polycrystals during high temperature plastic deformation, J. Mech. Phys. Solids 52 (6) (2004) 1289–1317.

[24] Kwai S. Chan, S.R. Bodner, D.E. Munson, A.F. Fossum, A constitutive model for representing coupled creep, fracture, and healing in rock salt, Technical Report, Sandia National Labs, Albuquerque, NM (United States), 1996.

[25] K.S. Chan, S.R. Bodner, D.E. Munson, Application of isochronous healing curves in predicting damage evolution in a salt structure, Int. J. Damage Mech. 9 (2) (2000) 130–153.

[26] Zhengmeng Hou, Mechanical and hydraulic behavior of rock salt in the excavation disturbed zone around underground facilities, Int. J. Rock Mech. Min. Sci. 40 (5) (2003) 725–738.

[27] Cheng Zhu, Chloé Arson, A model of damage and healing coupling halite thermo-mechanical behavior to microstructure evolution, Geotech. Geol. Eng. 33 (2) (2015) 389–410.

[28] Xianda Shen, Chloé Arson, An isotropic self-consistent homogenization scheme for chemo-mechanical healing driven by pressure solution in halite, Int. J. Solids Struct. 161 (2019) 96–110.

[29] Yang Liu, WaiChing Sun, Jacob Fish, Determining material parameters for critical state plasticity models based on multilevel extended digital database, J. Appl. Mech. 83 (1) (2016) 011003.

[30] Kun Wang, WaiChing Sun, Simon Salager, SeonHong Na, Ghonwa Khaddour, Identifying material parameters for a micro-polar plasticity model via X-ray micro-computed tomographic (CT) images: lessons learned from the curve-fitting exercises, Int. J. Multiscale Comput. Eng. 14 (4) (2016).

[31] Kun Wang, WaiChing Sun, Qiang Du, A cooperative game for automated learning of elasto-plasticity knowledge graphs and models with AI-guided experimentation, Comput. Mech. (2019) 1–33.
[32] Yujie Wei, Lallit Anand, On micro-cracking, inelastic dilatancy, and the brittle-ductile transition in compact rocks: A micro-mechanical study, Int. J. Solids Struct. 45 (10) (2008) 2785–2798.
[33] Peter K Kang, Marco Dentz, Tanguy Le Borgne, Ruben Juanes, Anomalous transport on regular fracture networks: Impact of conductivity heterogeneity and mixing at fracture intersections, Phys. Rev. E 92 (2) (2015) 022148.
[34] Martin Tjioe, Ronaldo I. Borja, Pore-scale modeling of deformation and shear band bifurcation in porous crystalline rocks, Internat. J. Numer. Methods Engrg. 108 (3) (2016) 183–212.
[35] Guang Liu, WaiChing Sun, Steven M Lowinger, ZhenHua Zhang, Ming Huang, Jun Peng, Coupled flow network and discrete element modeling of injection-induced crack propagation and coalescence in brittle rock, Acta Geotech. 14 (3) (2019) 843–868.
[36] Krishna Garikipati, Lori Bassman, Michael Deal, A lattice-based micromechanical continuum formulation for stress-driven mass transport in polycrystalline solids, J. Mech. Phys. Solids 49 (6) (2001) 1209–1237.
[37] Aurélien Villani, Esteban P Busso, Kais Ammar, Samuel Forest, MGD Geers, A fully coupled diffusional-mechanical formulation: numerical implementation, analytical validation, and effects of plasticity on equilibrium, Arch. Appl. Mech. 84 (9–11) (2014) 1647–1664.
[38] Aurélien Villani, Esteban P. Busso, Samuel Forest, Field theory and diffusion creep predictions in polycrystalline aggregates, Modelling Simulation Mater. Sci. Eng. 23 (5) (2015) 055006.
[39] François Renard, Dominique Bernard, Xavier Thibault, Elodie Boller, Synchrotron 3D microtomography of halite aggregates during experimental pressure solution creep and evolution of the permeability, Geophys. Res. Lett. 31 (7) (2004).
[40] Kun Wang, WaiChing Sun, An updated Lagrangian LBM–DEM–FEM coupling model for dual-permeability fissured porous media with embedded discontinuities, Comput. Methods Appl. Mech. Engrg. 344 (2019) 276–305.
[41] Chuanqi Liu, WaiChing Sun, Shift boundary material point method: an image-to-simulation workflow for solids of complex geometries undergoing large deformation, Comput. Part. Mech. (2019) 1–18.
[42] Luv Sharma, Ron HJ Peerlings, Pratheek Shanthraj, Franz Roters, Marc GD Geers, FFT-Based interface decohesion modelling by a nonlocal interphase, Adv. Model. Simul. Eng. Sci. 5 (1) (2018) 7.
[43] L Sharma, RHJ Peerlings, P Shanthraj, F Roters, MGD Geers, An FFT-based spectral solver for interface decohesion modelling using a gradient damage approach, Comput. Mech. (2019) 1–15.
[44] Ronaldo I. Borja, Conservation laws for three-phase partially saturated granular media, in: Unsaturated Soils: Numerical and Theoretical Approaches, Springer, 2005, pp. 3–14.
[45] Kun Wang, WaiChing Sun, A multiscale multi-permeability poroplasticity model linked by recursive homogenizations and deep learning, Comput. Methods Appl. Mech. Engrg. 334 (2018) 337–380.
[46] Morton E. Gurtin, Generalized Ginzburg–Landau and Cahn–Hilliard equations based on a microforce balance, Physica D 92 (3–4) (1996) 178–192.
[47] Martin Tjioe, Ronaldo I. Borja, On the pore-scale mechanisms leading to brittle and ductile deformation behavior of crystalline rocks, Int. J. Numer. Anal. Methods Geomech. 39 (11) (2015) 1165–1187.
[48] Bin Li, Christian Peco, Daniel Millán, Irene Arias, Marino Arroyo, Phase-field modeling and simulation of fracture in brittle materials with strongly anisotropic surface energy, Internat. J. Numer. Methods Engrg. 102 (3–4) (2015) 711–727.
[49] Bin Li, Corrado Maurini, Crack kinking in a variational phase-field model of brittle fracture with strongly anisotropic surface energy, J. Mech. Phys. Solids 125 (2019) 502–522.
[50] Ran Ma, WaiChing Sun, FFT-Based solver for higher-order and multi-phase-field fracture models applied to strongly anisotropic brittle materials and poly-crystals, Comput. Methods Appl. Mech. Eng. (2020).
[51] Morton E. Gurtin, Eliot Fried, Lallit Anand, The Mechanics and Thermodynamics of Continua, Cambridge University Press, 2010.
[52] Lallit Anand, A thermo-mechanically-coupled theory accounting for hydrogen diffusion and large elastic–viscoplastic deformations of metals, Int. J. Solids Struct. 48 (6) (2011) 962–971.
[53] A. Salvadori, R. McMeeking, D. Grazioli, M. Magri, A coupled model of transport-reaction-mechanics with trapping. Part I–Small strain analysis, J. Mech. Phys. Solids 114 (2018) 1–30.
[54] Florian K. Lehner, A model for intergranular pressure solution in open systems, Tectonophysics 245 (3–4) (1995) 153–170.
[55] Lallit Anand, Single-crystal elasto-viscoplasticity: application to texture evolution in polycrystalline metals at large strains, Comput. Methods Appl. Mech. Engrg. 193 (48–51) (2004) 5359–5383.
[56] Jaroslav Vondřejc, Jan Zeman, Ivo Marek, An FFT-based Galerkin method for homogenization of periodic media, Comput. Math. Appl. 68 (3) (2014) 156–173.
[57] Mark Messner, Armand Beaudoin, Robert Dodds, Consistent crystal plasticity kinematics and linearization for the implicit finite element method, Eng. Comput. 32 (6) (2015) 1526–1548.
[58] Ran Ma, Timothy J. Truster, FFT-Based homogenization of hypoelastic plasticity at finite strains, Comput. Methods Appl. Mech. Engrg. (2019).
[59] S. Kok, Armand Joseph Beaudoin, Daniel A. Tortorelli, A polycrystal plasticity model based on the mechanical threshold, Int. J. Plast. 18 (5–6) (2002) 715–741.
[60] Nathan R. Barton, Athanasios Arsenlis, Jaime Marian, A polycrystal plasticity model of strain localization in irradiated iron, J. Mech. Phys. Solids 61 (2) (2013) 341–351.
[61] Thomas Driesner, Christoph A. Heinrich, The system H_2O–NaCl. Part I: Correlation formulae for phase relations in temperature–pressure–composition space from 0 to 1000 C, 0 to 5000 bar, and 0 to 1 XNaCl, Geochim. Cosmochim. Acta 71 (20) (2007) 4880–4901.
[62] S. Teichtmeister, D. Kienle, F. Aldakheel, M.-A. Keip, Phase field modeling of fracture in anisotropic brittle solids, Int. J. Non-Linear Mech. 97 (2017) 1–21.

[63] Jan Zeman, Jaroslav Vondřejc, Jan Novák, Ivo Marek, Accelerating a FFT-based solver for numerical homogenization of periodic media by conjugate gradients, J. Comput. Phys. 229 (21) (2010) 8065–8071.
[64] Sébastien Brisard, Luc Dormieux, FFT-Based methods for the mechanics of composites: A general variational framework, Comput. Mater. Sci. 49 (3) (2010) 663–671.
[65] Jan Zeman, Tom WJ de Geus, Jaroslav Vondřejc, Ron HJ Peerlings, Marc GD Geers, A finite element perspective on nonlinear FFT-based micromechanical simulations, Internat. J. Numer. Methods Engrg. 111 (10) (2017) 903–926.
[66] Julian Kochmann, Stephan Wulfinghoff, Lisa Ehle, Joachim Mayer, Bob Svendsen, Stefanie Reese, Efficient and accurate two-scale FE-FFT-based prediction of the effective material behavior of elasto-viscoplastic polycrystals, Comput. Mech. 61 (6) (2018) 751–764.
[67] Julian Kochmann, Kiran Manjunatha, Christian Gierden, Stephan Wulfinghoff, Bob Svendsen, Stefanie Reese, A simple and flexible model order reduction method for FFT-based homogenization problems using a sparse sampling technique, Comput. Methods Appl. Mech. Engrg. 347 (2019) 622–638.
[68] Nathan R Barton, Joel V Bernier, Ricardo A Lebensohn, Donald E Boyce, The use of discrete harmonics in direct multi-scale embedding of polycrystal plasticity, Comput. Methods Appl. Mech. Engrg. 283 (2015) 224–242.
[69] Jingzhi Zhu, Long-Qing Chen, Jie Shen, Veena Tikare, Coarsening kinetics from a variable-mobility Cahn–Hilliard equation: application of a semi-implicit fourier spectral method, Phys. Rev. E 60 (4) (1999) 3564.
[70] Neville L. Carter, Hugh C. Heard, Temperature and rate dependent deformation of halite, Amer. J. Sci. 269 (3) (1970) 193–249.
[71] C. Barry Carter, M. Grant Norton, Ceramic Materials: Science and Engineering, Springer Science & Business Media, 2007.
[72] R. Quey, P.R. Dawson, F. Barbe, Large-scale 3D random polycrystals for the finite element method: Generation, meshing and remeshing, Comput. Methods Appl. Mech. Engrg. 200 (17–20) (2011) 1729–1745.